UNIVERSITÀ DEGLI STUDI DI PADOVA

UNIVERSITY OF PADUA

DEPARTMENT OF INDUSTRIAL ENGINEERING

MASTER'S DEGREE IN CHEMICAL AND PROCESS ENGINEERING

Master's degree Thesis in

Chemical and Process Engineering

Study on tri-component $Ru/NbOPO_4/TiO_2$ catalyst for the hydrodeoxygenation of depolymerized lignin products into valuable products.

Supervisor: Prof. Paolo Canu

Host institution supervisor: Prof. Jyri-Pekka Mikkola

Graduating Student: Giacomo Gorza

2052496

Academic Year 2022/2023

Abstract

Lignin, a complex and abundant biopolymer, represents a significant challenge in the paper industry as it is often considered waste material. However, lignin possesses immense potential as the first natural source of aromatic components, which can be harnessed to produce valuable dehydrogenated products. The focus of this study is the synthesis of a three-component acidic heterogeneous catalyst containing Nb, Ti, and Ru and its application in the lignin conversion into valuable dehydrogenized products. The catalyst preparation was first carried out at different acidity conditions in the preparation solutions.

Afterwards, the structure of the support and of the loaded particles were characterized with analytical techniques. N_2-phisysisorption was used to understand the surface area of the catalysts, NH_3-TPD for determining the acidity of the catalyst, XRD, SEM-EDX, FT-IR and TEM to understand the structure the catalyst had after the preparation at different acidity conditions.

The catalytic activity was studied in a batch reactor at different temperatures and reaction times to have a complete knowledge on the efficiency of the catalyst itself, using eugenol as reference reactant. It showed a good breaking of the methoxy group in the reactant, as well as the hydrogenation of the unsaturated C-C and -OH bonds. Regarding the structure of the catalyst: metallic Ru contributed to the increase of the acidity of the catalyst with a correspondent increase in Lewis's acid sites; TiO_2 contributed increasing the stability in the different reaction conditions while $NbOPO_4$ improved the selectivity towards the cleavage of the -OH and the hydrogenation of the aromatic ring.

A kinetic study was carried out to identify the reaction mechanism, a rate law, and compute the partial reaction order.

Table of contents

Introduction

Lignin is considered the most present biopolymer on the earth and one of the richest sources of aromatic compounds of the planet. The paper industry generates large quantities of lignin as a byproduct during the pulping process. Historically, lignin has been primarily considered a low-value material, often burned for energy recovery, or discarded as waste. However, the increasing demand for sustainable and renewable resources has prompted researchers to explore lignin's untapped potential as a precursor for high-value chemicals and fuels. Lignin, as a natural polymer, is composed of phenolic compounds interconnected through various types of chemical bonds, including C-O and C-C bonds. These linkages, along with the presence of hydroxyl (-OH) groups, present a challenge when attempting to convert lignin into valuable dehydrogenated products. Therefore, the development of an efficient and selective catalytic system is crucial to overcome these obstacles.

For these purposes the aim of this research is the development and the study of the potential of a tricomponent $Ru/NbOPO_4/TiO_2$ catalyst that has emerged as a promising candidate for the conversion of lignin into valuable products by investigating the catalytic properties of the catalyst, the efficiency and selectivity towards eugenol conversion, used as a reference reactant. Eugenol has been used for the presence of the methoxy functional group, the -OH bond as well as the double carbon bond that make it the closest chemical to lignin monomers in terms of functional groups.

This catalyst combines the advantages of ruthenium (Ru) as an active metal, niobium phosphate ($NbOPO_4$) as a Lewis and Bronsted acid sites provider, and titanium dioxide (TiO_2). By harnessing the unique properties of each component, this catalyst offers a synergistic effect, enabling the cleavage of C-O bonds, C-C bonds, and -OH bonds present in lignin. The presence of Lewis acid sites on $NbOPO_4$ facilitates the activation of lignin by promoting the breaking of C-O and C-C bonds. These Lewis acid sites act as electron acceptors, enhancing the catalytic activity of the overall system. Simultaneously, the Bronsted acid sites provide proton donors, facilitating the cleavage of -OH bonds and subsequent dehydrogenation reactions.

The study is subdivided into four chapters:

- *Chapter 1*: gives information about lignin characteristics and its usage in the industry. It also explores new paths for the lignin recycling and utilization.
- *Chapter 2*: describes all the materials, methods and tools that were used during the synthesis and the characterization of the catalyst.

- *Chapter 3*: provides knowledge about the catalyst synthesis procedure throughout all the steps and the characterization of every catalyst intermediate.
- *Chapter 4*: describes the catalytic activity of the catalysts and provides a basic kinetic study, conducted to study the reaction rate.

This project was carried out partly at *Chemistry Department of Umeå University*, in the research group of Professor Jyri-Pekka Mikkola. The experimental tests were carried out with the supervision of Dr. Ajaikumar Samikannu. PhD student Mihn Van Din contributed to the catalyst characterization in all the analysis. The last part of the work regarding the kinetic study and the writing of the thesis was done at *University of Padua* under the supervision of Professor Paolo Canu.

Chapter 1

Lignin characteristics and industry utilization

In this first chapter, a general overview of the lignin utilization at industry level is presented. It is followed by a discussion on its recycling strategies. The principal catalytic reaction for lignin conversion into valuable products studied nowadays are then introduced. To conclude the chapter the aim of this thesis is reported.

1.1 Lignin

1.1.1 Lignin types and functional groups[1-3]

Lignin is a natural polymer that has mechanical, antimicrobial, and antioxidant properties. It has the potential to produce numerous chemicals and biofuels currently of interest in the market. However, its heterogenous and complicated structure, along with the difficult extraction processes can slow down the research on its transformation into high-value materials.
Lignin is mostly present within lignocellulose biomass. This biomass is mostly composed of 44% to 50% of cellulose, of 28% to 31% of hemicellulose and of 15% to 25% of lignin, as exemplified in *Figure 1.1*.

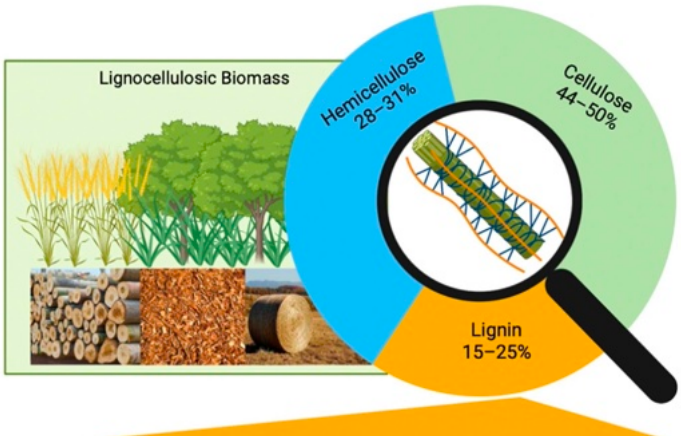

Figure 1.1 – Lignocellulose biomass components.[3]

1.1.1.1 Main lignin components

Lignin is a polymer with a three-dimensional network in which phenylpropane units, the main components, are connected by the asymmetrical connection of C-C and C-O bonds. The three phenyl propane monomers of lignin structure are a guaiacyl monomer (denoted as G type) derived from coniferyl alcohol, syringyl monomer (denoted as S type) derived from syringyl alcohol, and p-phenyl monomer (denoted as H type) derived from coumaryl alcohol.

The quantity of lignin changes between the different types of lignocellulosic biomass. It decreases from softwoods to hardwoods and then to grasses. Along with the lignin, the percentage of G, H, and S groups can vary considering the different biomasses.

In hardwood lignin, syringyl units are found in the highest amount up to 58.10%, and guaiacyl-type compounds are around 18.75%. In softwood lignin, instead, guaiacyl-type units are the ones present in the highest amount. Finally, in grasses, there is a nearly equal amount of syringyl type units and guaiacyl type units.

The chemical structure of lignin is still not defined in detail because of its complexity. Research has involved spectroscopy, thermos-gravimetric analysis, computational studies along with NMR techniques to best define the structure, the main monomers and bonds present.

The bonds between the monomers in lignin are mostly of type β-O-4, α-O-4, and 4-O-5, as well as C-C bonds like β-1, β-5, 5-5, and β-β. Their percentage depends again on the difference between biomasses. In most of the cases, lignin presents around two-third C-O-C bonds and one-third are C-C types. The main bond types contain 48%-60% β-O-4 linkages and roughly 25% 5-5 bonds. All the linkages are shown in *Figure 1.2.*

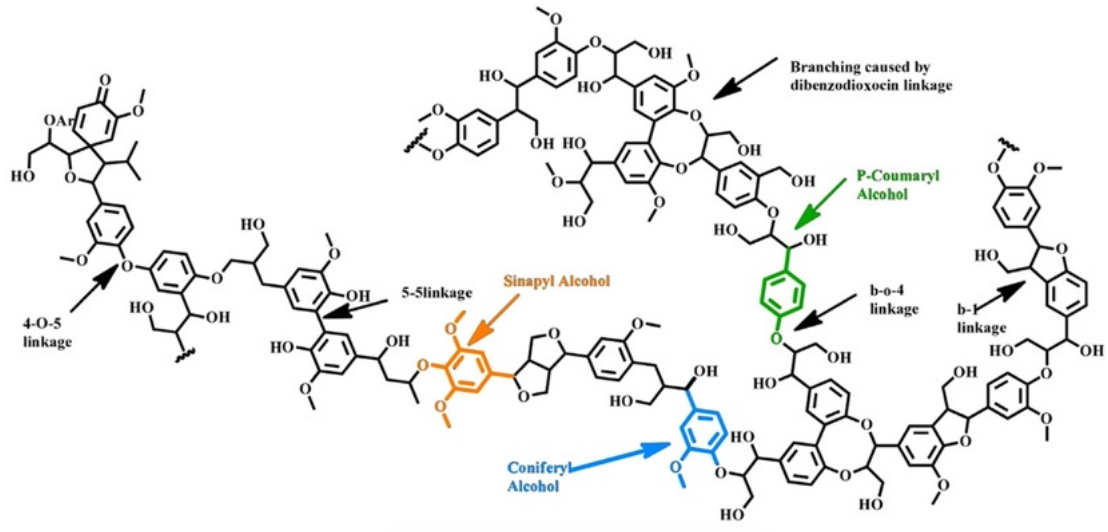

Figure 1.2 – Lignin structure with the different types of bonding and monomers.[2]

1.1.1.2 Typologies of lignin

The biomass pretreatment methods define the differences between the lignin types, regarding the chemical and physical properties. Lignin can be classified in mainly four categories based on these methods: Kraft lignin, a by-product mainly of pulp and paper industries, derives from the kraft process. It is highly condensed, meaning that the polymers are closely packed together, forming a denser structure, with strong ether and C-C bonds. It contains sulfur impurities that can compromise its utilization due to the toxic nature of the compound. Kraft lignin also contains a high number of phenolic groups, with a small amount of ash and carbohydrates.
Soda lignin, also known as alkaline lignin, is obtained from the soda pulping process. In this method, biomass is treated with a solution of sodium hydroxide (NaOH) or other alkaline chemicals under elevated temperatures and pressures. Unlike kraft and lignosulfonate lignin, soda lignin is sulfur-free. It is more condensed due to the severe pulping conditions, with minor amounts of ash and carbohydrates.
Lignosulfonate lignin is derived from the sulfite process. This type of lignin is water-soluble and has specific colloidal properties. It can be used as a stabilizer, dispersing agent, surfactant, or adhesive.
Lignin in the biomass can be dissolved in the organic solvent; the lignin recovered from the liquid is called organosolv lignin. The structure of organosolv lignin is close to native lignin and contains easily breakable aryl-ether linkages (β-O-4). It has a homogeneous structure with low molecular weight and polydispersity. Organosolv lignin is highly pure, with very low amounts of carbohydrates and ash.

1.1.2 Lignin as an industrial waste[4-7]

Lignocellulosic biomass is the primary source from which lignin is obtained. Total dry biomass is produced by forest and agricultural lands. This biomass has different purposes in biorefineries, power plants, and the pulp and paper industries, leading to the generation of energy and chemicals. However, the pulp and paper industries are responsible for producing approximately 30% of the lignin within lignocellulosic biomass. Similarly, sugar industries also contribute to lignocellulosic waste, containing from 25% to 30% of lignin. Nowadays, biorefineries utilize mostly the cellulose and hemicellulose compounds of lignocellulosic biomass to manufacture valuable products, such as butanol, ethanol, levulinic acid, furfural and furfuryl alcohol. This leaves lignin as a residual waste. The pulp and paper industries generate a huge amount of around 50 to 70 million tons of lignin each year, and some projections estimate an increase of 62 million tons per year from the expanding biofuels sector. Some researchers even anticipate that this number could reach 225 million tons per year by 2030.

1.2 Lignin valorization methods[8]

1.2.1 Present applications

Lignin valorization is an active field of research and has shown promising results at the experimental scale. However, these applications struggle to reach the industrial state, due to practical limitations. The current fields in which lignin is involved can be summarize in the following applications.

Heat and power energy supply: Lignin is often burned to generate heat and electricity. Almost 98% of the lignin produced is used for this purpose. The energy content of dry lignin is around 25 MJ/kg, which is comparable to the energy density of coal (24–30 MJ/kg). Co-firing lignin with coal in pulping boilers has been a common practice: it leads to an improvement in the boiler efficiency by up to 38% compared to using only coal. This coupling also reduces carbon emissions by 60%.

Lignin as binder: water-soluble lignin salts are useful as binders in water-based pigment printing processes. Binders derived from lignin are used in coal briquettes, ceramics, mineral dust briquetting, and boards.

Lignin as cement: Low level of lignin or modified lignin has been found to improve concrete's strength, grinding ease, and resistance to moisture and acid rain damage, giving lignin-derived cement a real economic advantage. Sulfonation processes can add sulfate groups to lignin, making it act as a dispersant in cement.

Pyrolysis and syngas products: lignin is involved in pyrolysis to produce solid biochar, bio-oils, or gases. The resulting products depend on temperature, heating rates, and additives.

Gasification is a key method for lignin valorization, producing a mixture of hydrogen, carbon monoxide, and small amounts of carbon dioxide (syngas), which can be used in various processes.

1.2.2 Under study applications

Chemical processing of lignin gives several opportunities to transform it into valuable chemicals useful in various industrial fields. These processes include lignin depolymerization, synthesis of active chemical sites and functionalization of hydroxyl groups.

Between the lignin’s different applications, it has the potential to be a low-cost and less pollutant alternative for carbon fiber production. Lignin-based carbon fibers are being included in sports, aerospace, and automotive manufacturing, where they replace traditional steel components.

Additionally, lignin can be converted into phenolic compounds through various processes such as hydroxyalkylation, demethylation, phenolation, and methylolation. These phenolic compounds, thanks to the presence of hydroxyl groups, are highly reactive and can easily be

oxidized and polymerized. This characteristic is being applied to synthesize adhesives, resins, and composites that can either replace or complement traditional phenol-formaldehyde resins, resulting in adhesives with low free formaldehyde content and improved environmental performance.

Besides, lignin oxidation processes carry out substances like aldehydes, various acids, and dimethyl sulfoxide (DMSO) and vanillin, a widely used flavoring agent in food, beverages, and pharmaceuticals. Lignin-derived vanillin is expected to reduce the volatility of the natural vanilla market. The methods for achieving this oxidation include organometal-catalyzed oxidation, biomimetic oxidation, enzyme-based oxidation, and organic solvent nanofiltration.

Lignin can also be employed as a raw material to produce environmentally friendly polyurethane resins. These resins have applications in industries such as shipbuilding, automotive manufacturing, furniture insulation, and packaging. Traditional polyurethane production relies on non-environmentally friendly diisocyanates and diols. Lignin polyurethane, on the other hand, is biodegradable and more eco-friendly. The process of creating polyurethanes involves the urethanization reaction, where hydroxyl groups react with isocyanate groups to form urethane linkages.

Lignin is also under study for its potential as a natural flame retardant and antioxidant in polymer systems. Studies have demonstrated that the presence of lignin can effectively reduce the flammability of polymers such as polypropylene, PBS, ABS, and PET. Moreover, lignin's aromatic character makes it an effective antioxidant, with functional groups capable of finding free radicals, terminating oxidative propagation reactions, and enhancing oxidative stability. Lignin nanoparticles exhibit better antioxidant and UV-protection properties, making them important in industries such as cosmetics, pharmaceuticals, and food.

Furthemore, lignin can be utilized as sequestering agent. It possesses the capability to capture metal ions and form complexes, especially in the form of lignosulphonates. This property makes it useful for soil improvement and conditioning, and the removal of harmful metals. Moreover, lignin has been evaluated as a controlled-release agent for herbicides, pesticides, and fertilizers in agriculture and forestry operations. Lignin hydrogels have been tested as water-storing soil conditioners in agriculture and forestry and have shown potential in wastewater treatment by absorbing contaminants and removing dyes.

In addition, lignin is explored for use in energy storage devices, offering opportunities to improve efficiency, reduce toxicity, cost, and environmental impact. It has been studied for applications in lead-acid batteries, electrochemical capacitors, supercapacitors, solar cells, and fuel cells. Notably, lignin can serve as a low-cost cathode-active material for primary lithium batteries, potentially replacing toxic and non-renewable elements. These materials are being developed for use in various energy storage devices, promoting sustainability in the energy sector.

In the biomedical field, lignin products are being used in the development of biobased nanocarriers for delivering active bio-agents. Lignin nanoparticles are explored for various medical applications, including diagnostic and therapeutic purposes, tissue engineering, DNA delivery, and drug delivery systems. Lignin-based hydrogels and nanotubes have an important role in stem cell and cancer research, tissue engineering, immunomodulation, and in vitro diagnostics. They are also tested in drug delivery systems, wound care, and water purification, contributing to their growing importance in the biomedical field.
Finally, as one of its most important applications, lignin is a source of hydrocarbons through catalytic hydrogenolysis processes. The production of hydrocarbons from lignin is influenced by factors like processing temperature, catalysts, and feedstock. Fast pyrolysis processes can convert lignin into valuable hydrocarbons like benzene, toluene, and xylene (BTX), which have a wide range of applications. Producing BTX compounds from lignin necessitates the breakage of C-O and C-C bonds through depolymerization and hydrodeoxygenation.

1.3 Catalytic reactions for lignin conversion

1.3.1 Lignin depolymerization[9]

Lignin depolymerization is the first step towards the production of valuable products from the lignocellulosic feedstock. This project focuses on reductive depolymerization with H_2 gas used as hydrogen source. This process is also called hydroprocessing.
Within hydroprocessing, two subcategories are defined based on reaction temperature: mild (<320°C) and harsh hydroprocessing (>320°C). Mild hydroprocessing, conducted in a liquid phase with solvents and catalysts, while harsh hydroprocessing can be conducted without solvents.
Different catalysts have been used for depolymerization of lignin with external hydrogen gas; among them the most utilized were bi-functional catalysts containing noble metals like Pd, Pt, Ru, Rh, and transition metals like Ni. These catalysts were mostly Pd/C, Ni/C, Pt/C, Pt/Al_2O_3, Ru-based materials supported on SBA-15 or TiO_2, bimetallic NiRu, NiRh or NiPd. The main characteristic is that they can cleave C-O and C-C bonds, perform hydrodeoxygenation, and hydrogenate aromatic double bonds.
However, these reactions require severe conditions, including high temperatures (>280°C), which may lead to repolymerization reactions, especially with acidic catalysts, and high initial H_2 pressure (around 100 bars). Complete conversion is typically achieved only at very high reaction temperatures (>300°C).

1.3.2 Hydrodeoxygenation of depolymerized products[9-13]

Hydrodeoxygenation (HDO) is a chemical process used to remove oxygen from organic compounds. Its main application is on bio-derived feedstocks like lignin, biomass, or bio-oils. HDO is utilized to produce mainly hydrocarbons or other value-added products with lower or null oxygen content. It is a useful step in the conversion of biomass into biofuels, as oxygenated compounds are less energy-dense and can lead to inefficient combustion, deposits and fouling or an increase in pollutant emissions.

The catalyst in the HDO reaction is very important. It allows to reduce the reaction temperature and pressure and obtain higher conversion and yield. Previous experimental studies have shown that bi-functional catalysts are the preferred system for the HDO process. The structure of the catalyst involves an active metal, typically Pt, Ru, Ni or Pd and a catalyst support, a mesoporous material such as SBA-15 or TiO_2 or carbon.

The active metals have reducible capabilities for hydrogen activation and they promote the hydrogenation of aromatic rings or unsaturated compounds during the HDO process.

The role of the supports in the reaction is essential: they disperse and stabilize the active metal species. Moreover, the presence of Lewis and Brønsted acidity from catalyst supports allows a better cleavage of the C-O bonds, typically broken only at very high temperatures.

Previous studies have demonstrated that for the effective conversion of lignin monomers in the HDO process, elevated temperatures well above 200°C and pressures exceeding 50 bar are required in batch reactors, as indicated in the cited references.

1.4 Aim of the thesis[14]

This thesis work is dedicated to the development of a versatile catalyst with the capacity to serve two main purposes: first, depolymerizing lignin, and second, performing the hydrodeoxygenation of the depolymerized products. As demonstrated in [14], $Pd/NbOPO_4/SBA\text{-}15$ achieves high conversion and selectivity towards C-C bonds in the HDO reaction. In this study, Ru is employed as a noble metal along with $NbOPO_4$ to enhance the catalyst's acidity and investigate its behavior with respect to other lignin monomer bonds. TiO_2 is used as a support instead of SBA-15 since the latter, which is silica-based, is corroded by highly concentrated acid solutions, while TiO_2 is not and proves to be chemically more stable. The first focus is on optimizing the reaction conditions, specifically by reducing both the required temperature and pressure for these processes. Research has shown that achieving an ideal balance between Lewis and Brønsted acid sites within the catalyst enhances its efficiency in terms of conversion and selectivity, particularly under less severe temperature and pressure conditions. To achieve this, the catalyst was synthesized with varying concentrations of hydrochloric acid, as the acidity of the synthesis solution directly influences the ratio of these

distinct acid sites. The characterization of the catalysts and their intermediate supports was carried out to identify the best combination for achieving the most desirable final catalyst structure.

Given that this study focuses on converting lignin monomers into valuable products, after the characterization process, a series of hydrodeoxygenation reactions were conducted. Eugenol, with its methoxy functional group, -OH bond, and double carbon bond, closely resembling the functional groups found in lignin monomers, was selected as the reference reactant. This choice allows for a meaningful comparison and understanding of the catalyst's performance in lignin conversion.

Chapter 2
Materials and experimental methods

This chapter is focused on the description of the materials used for the synthesis of the catalyst and the various techniques employed. The different tools and instruments used for the catalyst characterization are also described.

2.1 Materials

2.1.1 Raw materials for $NbOPO_4$ production

2.1.1.1 Niobium chloride ($NbCl_5$)

Niobium chloride, supplied by *Sigma-Aldrich* as white powder (>99% purity), was used as one of the main reagents during the synthesis of $NbOPO_4$ as niobium provider. Some of the properties are listed below and its chemical structure is shown in *Figure 2.1:*

- Molecular weight: 270.17 g/mol;
- Melting point (@ 1 atm): 204.7°C;
- Boiling point (@ 1 atm): 248.2°C;
- Density (@ 25°C): 2.75 g/cm^3.

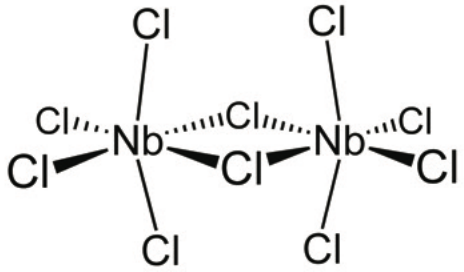

Figure 2.1 – Chemical structure of niobium chloride

2.1.1.2 Ammonium phosphate monobasic ($NH_4H_2PO_4$)

Ammonium phosphate monobasic, supplied by *VWR Chemicals* as white crystalline powder (>99% purity), was involved in the production of the $NbOPO_4$. It was used as phosphate donor.

In the *Figure 2.2* the chemical structure can be seen while some of the properties are listed below:

- Molecular weight: 115.03 g/mol;
- Melting point (@ 1 atm): 190°C;
- Boiling point (@ 1 atm): 197°C;
- Density (@ 25°C): 1.80 g/cm^3.

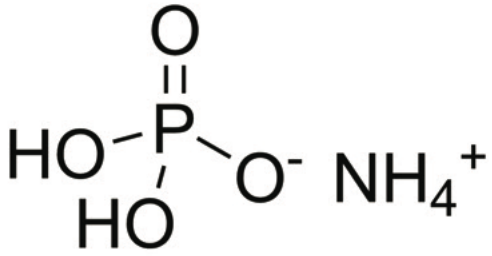

Figure 2.2 – Chemical structure of ammonium phosphate monobasic

2.1.1.3 Hydrochloric acid 37% (*HCl*)

Hydrochloric acid 37%, supplied by *VWR Chemicals*, is the most concentrated solution available commercially and is categorized as a strong acid. It was used as solvent at different concentrations not only during the synthesis of $NbOPO_4$ but also to produce the TiO_2 structure and the final catalyst. Some of the properties are recorder below:

- Molecular weight (pure *HCl*): 36.46 g/mol;
- Melting point (@ 1 atm): ~-28°C;
- Boiling point (@ 1 atm): ~50°C;
- Density (@ 25°C): 1.19 g/cm^3

2.1.2 Raw materials for TiO_2 production

2.1.2.1 P123

Poly(ethylene glycol)-block-poly(propylene glycol)-block-poly(ethylene glycol), also known as Pluronic® P123, provided by *Sigma-Aldrich*, is a non-ionic block polymer soluble in water for temperatures below ~15°C. It was used as template for the synthesis of TiO_2 support in order to obtain the desired mesoporous structure. Some properties are listed below and the chemical structure is presented in the *Figure 2.3*:

- Molecular weight: ~5800 g/mol;

- Boiling point (@ 1 atm): >149°C°C;
- Density (@ 25°C): 1.018 g/cm^3.

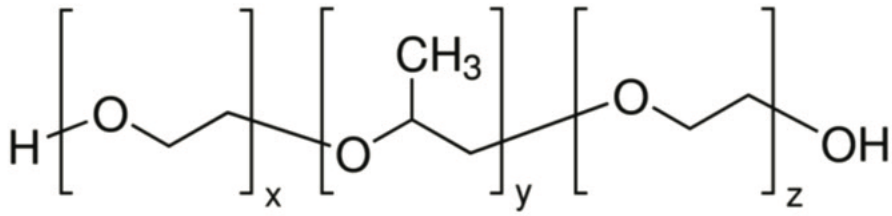

Figure 2.3 – Chemical structure of P123

2.1.2.2 Titanium isopropoxide (*Ti[OCH(CH$_3$)$_2$]$_4$*)

Titanium isopropoxide, supplied by *Sigma-Aldrich* (>97% purity), is an organometallic compound containing *Ti* as metallic atom. Its main utilization in the chemistry industry is as precursor in the synthesis of TiO_2. It was used for the same purpose also in this study. Some properties are recorded below, and the chemical structure is illustrated in *Figure 2.*4:

- Molecular weight: 284.22 g/mol;
- Melting point (@ 1 atm): 17°C;
- Boiling point (@ 1 atm): 232°C;
- Density (@ 25°C): 0.96 g/cm^3;
- Viscosity (@25°C): 4.5 cP.

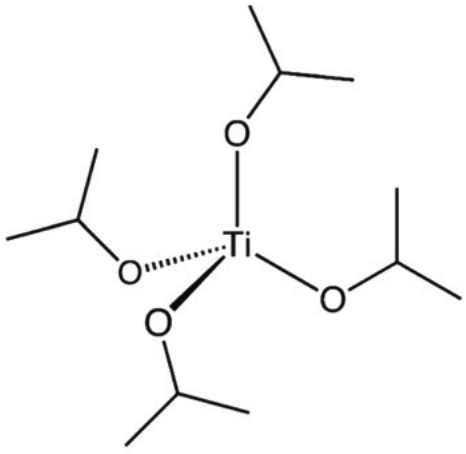

Figure 2.4 – Chemical structure of titanium isopropoxide

2.1.2.3 Absolute ehtanol (C_2H_6O)

Absolute ethanol, supplied by *VWR Chemicals* (>99.8% purity), has been utilized for as a solvent during the first steps of preparation of the TiO_2 support. Some properties are recorded below:

- Molecular weight: 46.07 g/mol;
- Melting point (@ 1 atm): -117°C;
- Boiling point (@ 1 atm): ~78°C;
- Density (@ 25°C): 0.79 g/cm^3;
- Viscosity (@25°C): 1.1 cP.

2.1.3 Raw materials for Ruthenium loading

2.1.3.1 Ruthenium(III) chloride hydrate ($RuCl_3 \bullet xH_2O$)

Ruthenium(III) chloride hydrate, provided by *Sigma-Aldrich*, is a black powder at ambient temperature. It was used to load the Ru on the $NbOPO_4/TiO_2$ structure. The properties and the chemical structure are respectively listed below in *Figure 2.5*.

- Molecular weight: 207.43 g/mol;
- Melting point (@ 1 atm): >500°C;
- Density (@ 25°C): 3.90 g/cm^3.

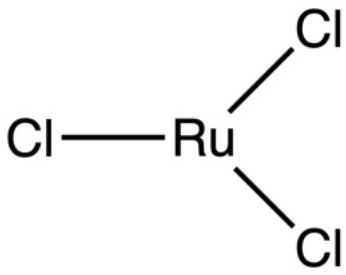

Figure 2.5 – Chemical structure of ruthenium chloride

2.1.4 Raw materials for HDO reaction

2.1.4.1 Eugenol ($C_{10}H_{12}O_2$)

Eugenol, supplied by *Sigma-Aldrich* (>99% purity), is an organic compound often used in food and fragrance industry. At ambient temperature it presents as yellow oil. It was used as reactant during the hydrodeoxygenation *(HDO)* reaction as model for the presence of the methoxy functional group, the -OH bond and the double carbon bond; same functional groups present in the lignin monomers.
Some properties are noted below and the chemical structure is shown in *Figure 2.6*.

- Molecular weight: 164.2 g/mol;
- Melting point (@ 1 atm): -7°C;
- Boiling point (@ 1 atm): 254°C;
- Density (@ 25°C): 1.07 g/cm^3;
- Viscosity (@ 25°C): 6.9 cP.

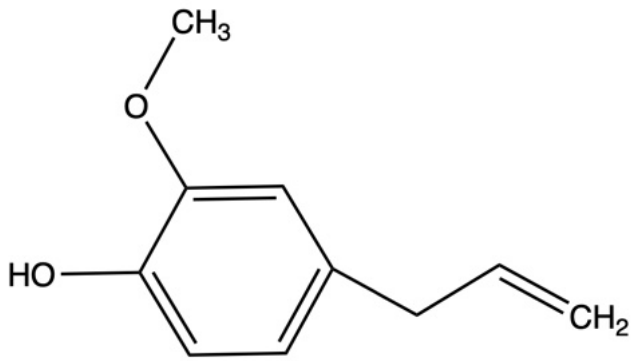

Figure 2.6 – Chemical structure of eugenol

2.1.4.2 Cycloexane (C_6H_{12})

Cycloexane, supplied by *Scharlab* (>99% purity), was used as solvent during the hydrodeoxygenation *(HDO)*. Some of the properties are presented below and the chemical structure is shown in *Figure 2.7*.

- Molecular weight: 84.16 g/mol;
- Melting point (@ 1 atm): 6.54°C;
- Boiling point (@ 1 atm): 80.72°C;
- Density (@ 25°C): 0.78 g/cm^3;

- Viscosity (@ 25°C): 1.0 cP.

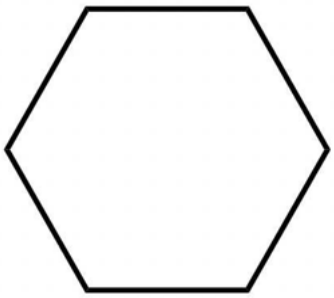

Figure 2.7 – Chemical structure of cyclohexane

2.2 Experimental methods

2.2.1.1 Vacuum filtration[15]

Vacuum filtration is a common method used to separate a solid from a liquid within a mixture. It is used especially when you need to separate a solid precipitate from a liquid, and it is useful because it is a quicker and more efficient separation compared to gravity filtration.
The vacuum filtration setup (*Figure 2.8*) consists in a Buchner funnel, filter paper, a filter flask, and a vacuum hose along with a vacuum pump. The Buchner funnel is shaped like a funnel and has a perforated plate at its base. A rounded piece of filter paper is placed inside the funnel, in order to cover the perforated plate completely without leaving any hole that could let the solution pass without being filtered.
The Buchner funnel is connected to the filter flask, which is attached to a vacuum pump via the vacuum hose.
To start the process, the vacuum pump is turned on, creating a pressure difference between the interior of the filter flask and the outside ambient, therefore creating a vacuum.
The solution mixture that contains both solid and liquid components is poured into the Buchner funnel. The mixture is forced to pass through the filter paper and the liquid part flows through it while the solid is collected on the filter paper as a residue.
The liquid is accumulated in the flask and then is disposed as needed.
The solid remains on the filter paper and is carefully removed with a spatula once the filtration is complete.
In this study, vacuum filtration played a crucial role in the preparation of the catalyst support and the final catalyst synthesis. After filtration, samples were separated from the solution, and any remaining water content was removed during the drying process.

Figure 2.8 – Vacuum filtration setup

2.2.1.2 Rotary evaporation[16]

Rotary evaporation, also known as *rotovap*, is a method used for slow removal of solvents from a sample under reduced pressure and controlled temperature. It consists of a round-bottom flask, containing the sample to be separated through evaporation, a water bath, a rotating flask, a condenser, a vacuum system, and a collection flask.

The process starts by placing the sample solution in the round-bottom flask which is placed in a water bath that is used to heat the mixture, or to cool it down in case of necessity. A vacuum pump is connected to the rotary evaporator for lowering the pressure in the system in order to reduce the boiling point of the solvent and facilitate the evaporation of the lighter component.

The round-bottom flask, known as the "*rotating flask*" is attached to the rotary evaporator and placed in a heated water bath. The temperature of the heating bath and the sample are controlled to prevent overheating or thermal degradation of the sample.

The rotation of the flask at a controlled speed, typically via a motor, is needed to increase the solvent's surface area exposed to the vacuum. Therefore, it accelerates the evaporation process.

In this study the rotation has not been applied since the component that needed to be removed was already very volatile.
Above the rotating flask, there is a condenser that is cooled with cold water. As the solvent evaporates from the sample in the rotating flask, it flows up as vapor and enters the condenser. The temperature of the condenser causes the vapor to condense back into a liquid phase. This liquid is then collected in a separate flask, which is known as the "*collection flask*". The solvent collected in the collection flask is further processed and disposed.
In order to obtain the optimum conditions during the separation temperature, rotational speed and vacuum pressure must be carefully set and checked during the process.
The pressure is controlled by the vacuum pump and is adjusted during the evaporating process to reduce the solvent's boiling point and to enable more efficient evaporation. Pressure must be applied or released to ensure the fully separation of the evaporated solvent avoiding the liquid contained in the rotating flask to go inside the condenser. The instrument can be seen in *Figure 2.9.*
In this study the “rotvap” was used to separate the HCl from the main solution containing the catalyst support powder.

Figure 2.9 – Rotary evaporation setup

2.2.1.3 Calcination[17]

Calcination is a thermal treatment process that involves heating a substance to high temperatures. It can be carried out aerobically (under oxygen flow) or anaerobically. The purpose of calcination is to remove volatile substances, chemically or physically transform a material, or remove impurities, leading to changes in the material's physical and chemical properties.

The process begins with selecting the material that needs to be calcined. In this project it consists in a solid powder. The material is then subjected to controlled heating in a specialized furnace in which the temperature and heating time are carefully controlled to achieve the desired outcome. The temperature can range from a few hundred degrees Celsius to over 1000°C; in this case the temperature never increased above 500°C.

After the desired calcination process is complete, the material is slowly cooled down to room temperature at a controlled rate since a fast cooling can sometimes result in undesired effects.

Calcination is used in a wide range of applications. In this study the main purposes of this step were the complete removal of the water content from the catalysts powder, the removal of organic impurities accumulated during the synthesis and the removal of the polymer support in the case of the TiO_2. In *Figure 2.10* the calcination oven can be seen.

Figure 2.10 – Calcination oven with samples

2.2.1.4 Hydrogen flow reduction

Hydrogen reduction is a chemical process that involves using hydrogen gas (H_2) to reduce a substance, typically by eliminating oxygen or other oxidizing elements. This reduction process is widely applied in various industrial and laboratory experiments, including the production of metals, the removal of oxygen from compounds, and the synthesis of catalysts.

The process starts with the selection of the substance that requires reduction. This substance is then combined with gaseous hydrogen (H_2) flow within a reaction vessel. Subsequently, the reaction vessel is heated to a specific temperature, often determined by the nature of the substance and reaction conditions. In a specific study it was heated at a temperature of 400°C. This heating is essential to provide the necessary activation energy for the reduction reaction to occur.

Gaseous hydrogen is continuously introduced into the reaction vessel. Hydrogen gas acts as a reducing agent, reacting with the oxidizing elements within the substance. The hydrogen molecule (H_2) contributes electrons, which are utilized to reduce the oxidation state or remove oxygen from the substance.

Inside the heated reaction vessel, the reduction reaction takes place. The oxidizing element within the substance accepts electrons from the hydrogen gas, leading to the removal of oxygen or a reduction in the oxidation state of the element. Consequently, this process effectively reduces the substance, resulting in a final product that typically contains fewer oxygen atoms or exhibits a lower oxidation state.

After the reduction reaction is complete, the resulting product is collected and stored separately from the original *"non-reduced"* compound.

It is very important to control the different reaction conditions, including temperature, pressure, and the flow of hydrogen gas. This control is essential for achieving the desired reduction while minimizing unwanted side reactions or alternate reaction pathways. A scheme of the hydrogen flow reduction can be seen in *Figure 2.11*. In this project this technique was used to remove all the oxygen content from the final catalyst.

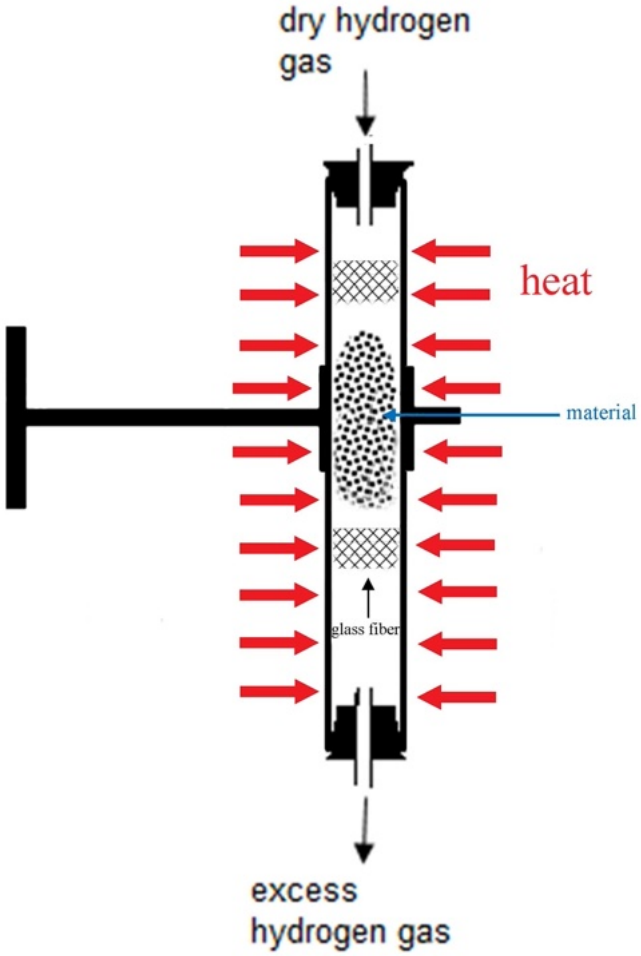

Figure 2.11 – Scheme of reduction reactor and vessel

2.3 Characterization techniques

2.3.1.1 BET method[18,19]

The BET (Brunauer, Emmett, and Teller) method is a technique in surface area analysis to determine the specific surface area of a solid material, in particular porous materials like catalysts, adsorbents, and powders. The name is given by its three developers, Stephen Brunauer, Paul Hugh Emmett, and Edward Teller.

The BET method is based on the physical adsorption of gas molecules into the surface of a solid material. The amount of gas adsorbed at various relative pressures is measured to calculate the specific surface area of the material.

During the BET surface area analysis, nitrogen is utilized due to its high purity and its strong affinity for solid materials. Since the interaction between gaseous and solid phases is typically

weak, the surface is cooled using liquid nitrogen (N_2) to make the adsorption process relevant. A precise amount of nitrogen gas is then incrementally introduced into the sample cell, creating conditions of partial vacuum to achieve relative pressures below atmospheric levels.

After the adsorption layers have formed, the sample is removed from the liquid nitrogen atmosphere and heated and the adsorbed nitrogen is released from the material. This released nitrogen is then quantified.

The data obtained is typically presented in the form of a BET isotherm, which graphically illustrates the amount of gas adsorbed and desorbed as a function of the relative pressure. There are five possible types of adsorption-desorption isotherms, each giving valuable information about the material's surface properties such as the pore size. Pore size classification includes micropores (below 2 nm), mesopores (between 2-50 nm), and macropores (above 50 nm). The isotherms are illustrated in the *Figure 2.12.*

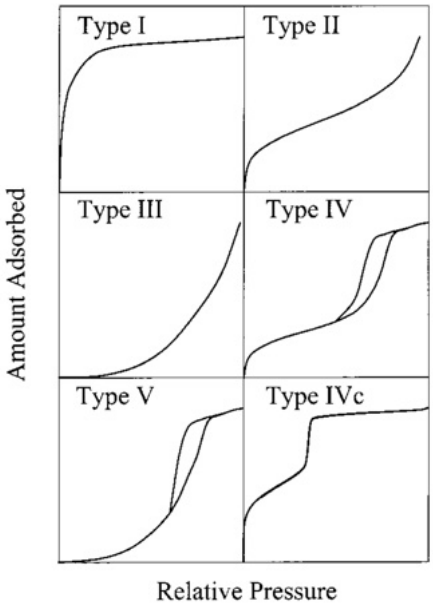

Figure 2.12 – BET isotherms.[18]

Type I isotherms show adsorption at low relative pressures. These isotherms are typical of micropores or monolayer adsorption due to strong adsorbent-adsorbate interactions. For nonpolar gases like nitrogen used in this project, Type I is typically associated with microporosity.

Type II and Type III isotherms come out when adsorption on macroporous solids leads to unrestricted multilayer formation, resulting in a gradual increase in adsorbed amount as the relative pressure rises. The adsorption and desorption branches coincide, causing no adsorption-desorption hysteresis.

Type IV and Type V isotherms are typical for mesoporous solids. These isotherms follow multilayer adsorption and are characterized by capillary condensation at higher pressures. Hysteresis loops may occur due to differences between capillary condensation and evaporation pressures.

In this work the specific surface areas were calculated using the BET method and the pore volumes were calculated from the corresponding desorption isotherms. The pore size distributions were estimated using the Barrett, Joyner and Halenda (BJH) algorithm using the built-in software from Micromeritics. The adsorption-desorption isotherms were recorded using Tristar 3000 apparatus, Micrometric Instrument Corp, Norcross, GA, USA, that can be seen in *Figure 2.13*, after outgassing the samples at 473 K for 3 h.

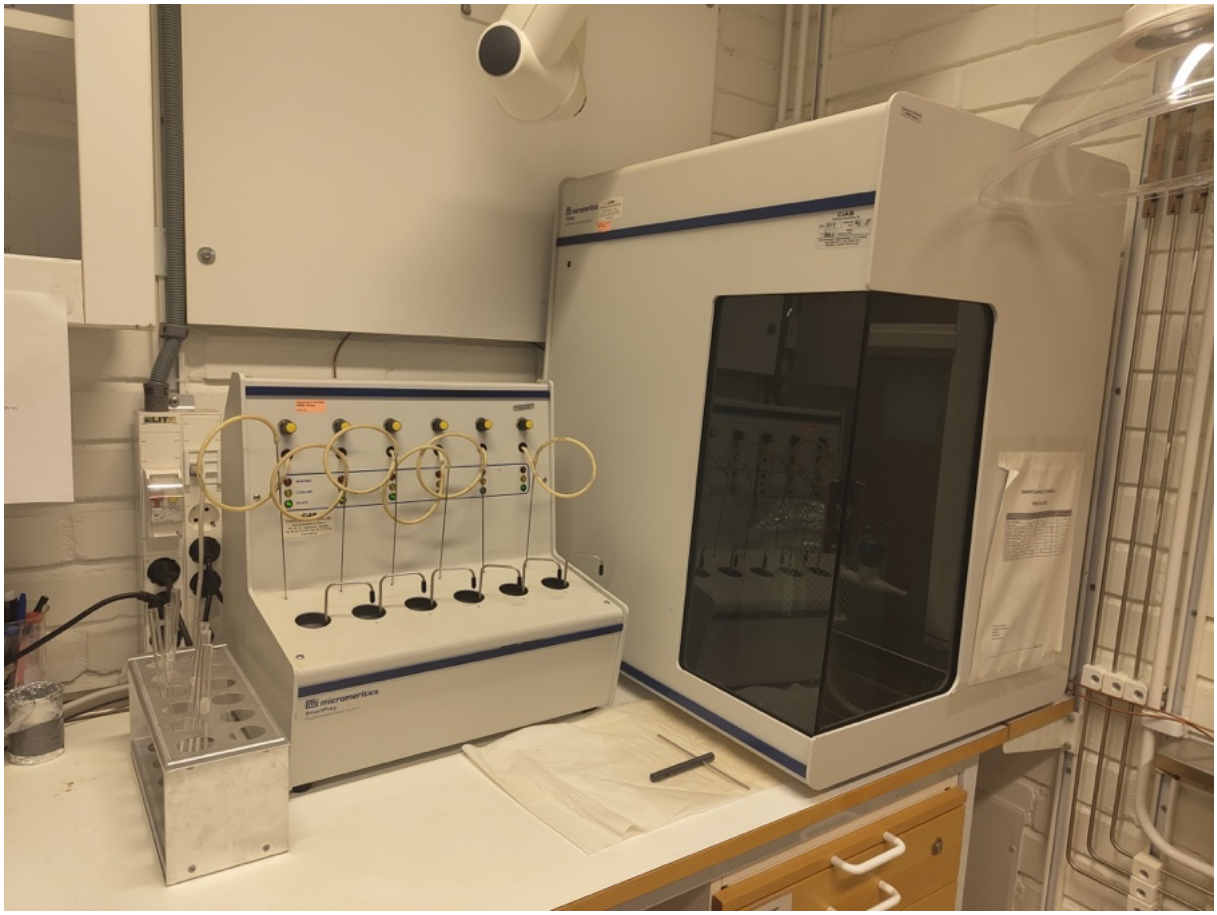

Figure 2.13 – Tristar 3000 apparatus utilized for BET analysis.

2.3.1.2 Temperature Programmed Desorption method

The determination of the total surface acidity of the catalysts was conducted utilizing the temperature-programmed desorption method (TPD). It is an analytical technique used in chemistry and materials science to study the desorption of gases or other species from solid

surfaces as a function of temperature. The instrument with which the analysis was carried out is BELCAT II from MicrotracBEL Corp. This method gives information about the acidity properties of the catalysts.

The procedure employed a probe molecule, 5% NH_3 in helium (He), to comprehensively assess the acidity of the catalyst surfaces.

In a typical TPD measurement, approximately 60 milligrams of the sample material were carefully placed within an adsorption vessel. To prepare the sample for analysis, it was subjected to an evacuation process at a temperature of 450°C for a duration of 2 hours under a continuous flow of helium (He). This step ensured the removal of any residual gases or contaminants.

Following the evacuation, the sample was cooled down to 100°C. The catalyst was then saturated with a mixture of 8.5% NH_3 in He for a period of 0.5 hours. This saturation step allowed for the precise assessment of the catalyst's reactivity toward ammonia. Then, the catalyst was flushed with He at 100°C for another 0.5 hours to eliminate any lingering traces of physically adsorbed ammonia molecules.

The TPD procedure was carried out within the temperature range of 100°C to 500°C. This involved ramping up the temperature at a controlled rate of 10°C per minute under a continuous flow of helium. During this process, the desorption of chemisorbed ammonia molecules from the catalyst's surface was recorded.

For accurate quantification, the amounts of chemisorbed and desorbed NH_3 were determined by referencing calibration curves that were established through the examination of varying volumes of NH3 in He. The instrumentation for the TPD analysis can be seen in *Figure 2.14.*

Figure 2.14 – BELCAT II instrument for TPD analysis.

2.3.1.3 X-ray Diffraction[20,21]

X-ray powder diffraction, also known as PXRD, is a technique used to determine the crystalline nature of the materials. The most common technique, and indeed the one utilized in this study is the powder X-ray diffraction (PXRD). It is a compact, advanced instrument as illustrated in *Figure 2.15*.

When X-rays interact with a crystal, they undergo diffraction, resulting in a distinct pattern that reflects the crystal's internal structure. In the case of powder X-ray diffraction, this diffraction pattern is acquired from a powdered sample rather than an individual crystal. This approach is more convenient and practical compared to single crystal diffraction, as it eliminates the need for isolated crystals. The diffraction pattern is graphically represented by plotting intensity against the detector angle which is typically equal to 2θ. The result of this process is given to as a diffractogram, in which the peak positions are influenced by the wavelength of the incident X-rays. In order to identify the different peaks on the diffractogram, it is necessary to use some database, to do a comparison between the obtained peak positions and the literature ones.

Diffractometers can be operated in both transmission and reflection configuration; the last one is the most common used. In the reflection mode, interactions between the incident X-ray beam

and the sample lead to the generation of intense reflected X-rays through constructive interference.

In this project Powder X-ray diffraction patterns of the catalysts were recorded on a PANalytical diffractometer using Cu Kα (λ =0.154 nm) radiation. The diffractograms were recorded in the 2θ range of 10 to 70° (wide-angle) in the steps of 0.0065652° with a time per step of 99.45s at each point.

Figure 2.15 – PANalytical diffractometer

2.3.1.4 Fourier Transform Infrared Spectroscopy[22,23]

Fourier Transform Infrared Spectroscopy, often abbreviated as FT-IR, is an analytical technique used in various scientific disciplines. It involves the interaction of the materials with infrared (IR) light, giving information about the chemical composition, molecular structure, and functional groups of different materials.

In FT-IR spectroscopy, a sample is exposed to a broad range of infrared wavelengths, and the IR light interacts with the molecules, causing them to vibrate. These vibrations correspond to

stretching and bending motions of the atoms in the molecule, and they occur at characteristic frequencies for different chemical bonds and functional groups.
FT-IR analysis measures the range of wavelengths in the infrared region that are absorbed by the material. The sample's ability to absorb the infrared light's energy at various wavelengths is measured to determine the material's molecular composition and structure. The resulting pattern of absorption peaks in the FT-IR spectrum provides information about the sample's chemical properties. The output of an FT-IR analysis is presented as an infrared spectrum, which displays peaks and troughs corresponding to the various vibrational modes of the sample. Each peak in the spectrum is associated with a specific vibrational frequency.
FT-IR spectroscopy has both qualitative and quantitative applications. Qualitatively, it is used to identify the chemical composition, highlight specific functional groups, and determine molecular structures within the sample. Quantitatively, it can be used to measure the concentration of specific compounds in a mixture.
The FT-IR was utilized to visualize the different bonds present in the catalyst and to highlight its crystalline or amorphous phase. The spectra were recorded on a Bruker spectrometer (Vetex 80) FT-IR over a range of 400-4000 cm^{-1} at a resolution of 2 cm^{-1} in ATR (attenuated total reflection) transmission mode. The instrument is shown in *Figure 2.16*.

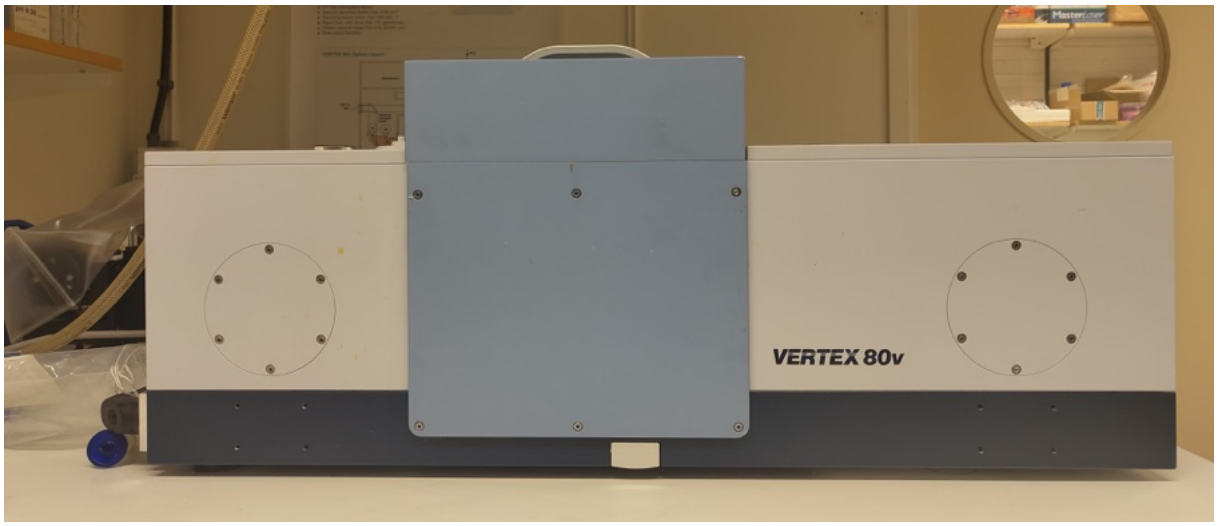

Figure 2.16 – Vetex 80 spectrometer.

2.3.1.5 Scanning Electron Microscope - Energy-dispersive X-ray[24-26]

Scanning Electron Microscope (SEM) is an electron microscope used in scientific research, materials science, biology, and various fields for obtaining high-resolution, three-dimensional images of nanoscale objects. It operates by utilizing a low-energy electron emitting beam to focus on and scan samples.

Its function involves using kinetic energy to produce signals by interacting with electrons. Among the different types of electrons produced, secondary electrons, backscattered electrons, and diffracted backscattered electrons are the important ones. The secondary electrons are needed to visualize the shape and surface of the specimen; the backscattered electrons instead reveal the contrast in composition of the elements. Finally, the diffracted backscattered electrons are used to see crystallized elements and photons.
SEM is frequently coupled with energy-dispersive X-ray (EDS or EDX) analysis to give chemical information through X-ray utilization.
In EDX analysis, the electron beam hits the inner shell of an atom, taking out an electron and creating a positively charged gap. This causes an electron from an outer shell to move in to fill the gap. As this electron moves from the outer shell, which has more energy, to the inner shell with less energy, it releases energy in the form of an X-ray. The energy of this X-ray corresponds to a specific element and its transition.
A silicon drift detector receives and collects these emitted X-rays, and a software interprets the data that then are displayed as a mapping.
EDS analysis is carried out for both qualitative and quantitative purposes, enabling users to identify the particles present and determine their concentration percentages in the sample. In this study the surface morphology and elemental composition of the catalytic materials were examined by field-emission scanning electron microscopy (FESEM, Carl Zeiss Merlin GmbH) operating at 5 kV, equipped with energy-dispersive X-ray spectroscopy (EDS, Oxford Instruments X-MAX 80 mm^2).

2.3.1.6 Transmission Electron Microscopy[27,28]

TEM stands for Transmission Electron Microscopy. It is a powerful imaging technique used in the field of microscopy and materials science to obtain high-resolution images and detailed information about the structure and morphology of extremely small objects (up to the order of 10^{-9} m). It utilizes a high-energy electron beam, which is directed through a sample. TEM substitutes electrons for light. Due to their substantially shorter wavelength compared to light, the achievable resolution for TEM images is higher by several orders of magnitude when compared to light microscopes. As a result, TEM can be used to analyze the internal structures, with a very high level of detail.
In the TEM setup, the electron gun emits a focused beam of electrons. This beam is narrowed and aligned by the condenser lens. The condenser aperture limits the beam by filtering out high-angle electrons. The beam then reaches the sample, and its passage depends on the sample's thickness and electron transparency. The portion that goes through is directed by the objective lens, creating an image on a phosphor screen. Optional objective apertures can be used to enhance contrast by blocking high-angle diffracted electrons. This resulting image travels

through the column, passing through intermediate and projector lenses, magnifying as it goes. Eventually, it strikes the phosphor screen, producing visible light for observation. Darker areas in the image indicate where fewer electrons passed through, while lighter areas show where more electrons traversed the sample.

In this project TEM analysis was needed to evaluate the uniform distribution of Ru over the $NbOPO_4/TiO_2$ structure.

Chapter 3
Catalyst synthesis and characterization

This chapter is focused on the experimental procedure and on the characterization of the synthetized catalyst. At first the preparation of the different materials and of the final catalyst are described. Secondly the characterizations through different techniques are presented.

3.1 Experimental procedure

3.1.1 Preparation of $NbOPO_4$ material[14]

$NbOPO_4$, denoted as NbP, was synthesized varying the concentration of hydrochloric acid. This was done to study the different characteristics in terms of surface area, porosity and crystallinity the catalyst develops when synthesized at different HCl conditions. The different molarities studied were from 1 molar to 12 molar and they are going to be denoted as 1M,3M,6M,9M and 12M.

The synthesis procedure consisted of: 3.976g of niobium chloride were dissolved in a 500 mL high-density polyethylene bottle (HDPE). The dissolution was carried out using a solution of 100mL of HCl and milli-Q water.

To ensure complete homogenization and uniformity, the resulting mixture was stirred for a duration of two hours under ambient room temperature conditions. Simultaneously, in a separate 500mL HDPE container, 3.3852g of ammonium phosphate monobasic ($NH_4H_2PO_4$) were dissolved in a solution consisting of 100mL of HCl and milli-Q water. Similarly, to the previous one, the mixture of $NH_4H_2PO_4$ and HCl proceeded to complete dissolution, resulting in a second homogeneous solution.

The following step involved the gradual addition of the second solution to the first. Then this solution was subjected to overnight stirring at a temperature of 80 °C.

Following the hydrolysis and acid-base reactions period, the stirring action was stopped, and the reaction mixture was maintained at a constant temperature of 80 °C for an additional three hours to promote the crystallization of the product.

After the conclusion of the crystallization phase, the resultant material was separated from the solution through a filtration process. The separated material was subsequently washed multiple times with deionized water to remove any residual impurities.

To achieve the desired material characteristics, a drying process was actuated on the filtered product. It was dried overnight at a temperature of 95 °C. Afterwards a calcination process was employed. This calcination process was conducted at a temperature of 450 °C for a period of 5 hours, under a controlled flow of air with a rate of 100 liters per hour.

3.1.2 Characterization of $NbOPO_4$ material

For the first intermediate, a comprehensive analysis was carried out using different techniques explored in *Section 2.3*.

3.1.2.1 BET

An important part of this study consisted in BET analysis to learn about the material's pores, surface area, pore size, and volume.
The data showed a consistent structural similarity among the 1M, 3M, and 6M samples. However, the 9M and 12M samples showed a significant change, indicating that the material's properties were different as the concentration of the synthesis solution increased.
The analysis of the isotherms, as detailed in *Section 2.3.1.1*, provided information on the porosity. The isotherms for the 1M, 3M, and 6M samples displayed a Type I pattern, indicative of a microporous structure within the material, as it can be seen in *Figure 3.1, Figure 3.2* and *Figure 3.3*. This evaluation was then confirmed by the pore size analysis, which gave average values of 2.60 nm, 2.70 nm, and 3.08 nm for the respective molarities.

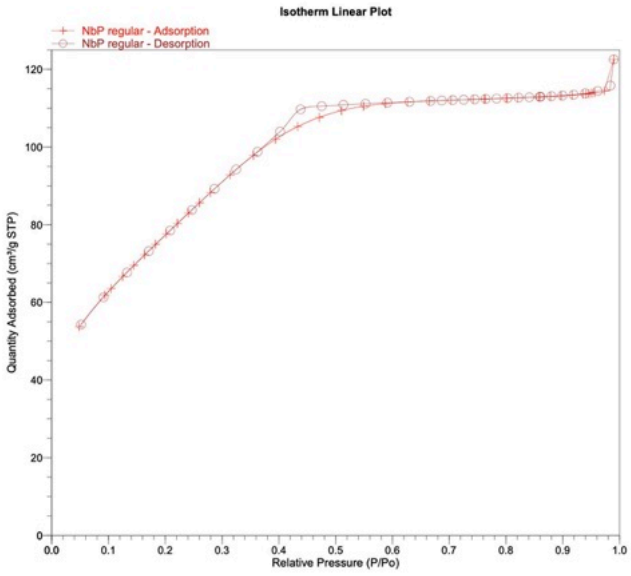

Figure 3.1– NbP 1M adsorption-desorption isotherm

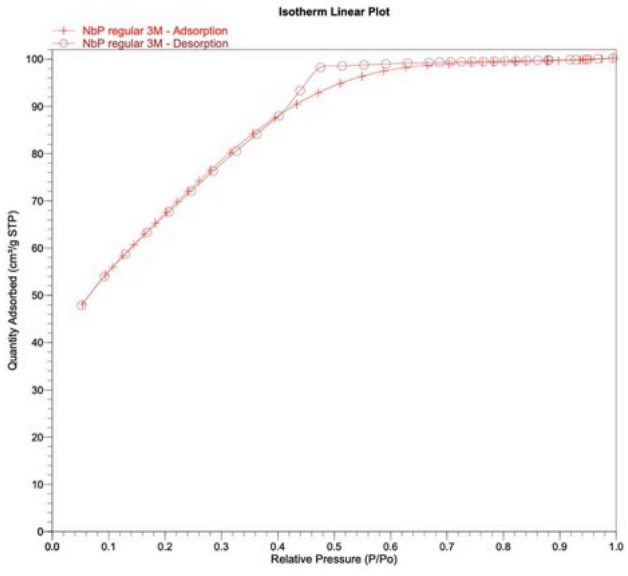

Figure 3.2– NbP 3M adsorption-desorption isotherm

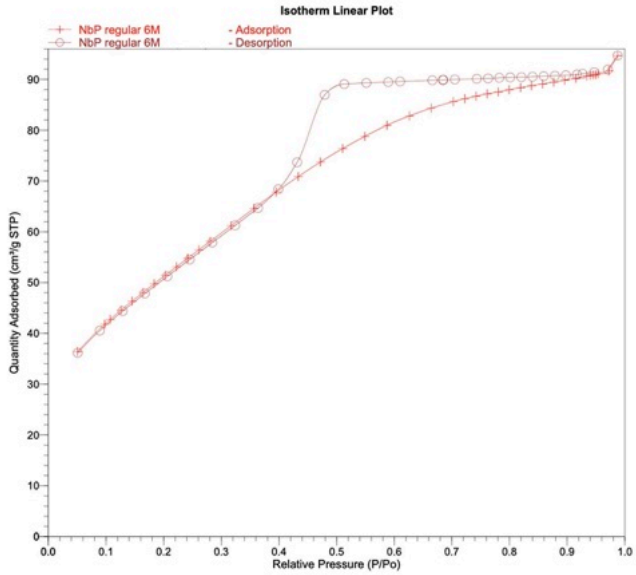

Figure 3.3– NbP 6M adsorption-desorption isotherm

The transition from a microporous to a mesoporous structure became clear in the 9M and 12M samples. This transformation is highlighted from the analysis of isotherm curves, in this case correspondent to a Type IV curve, clearly different from the Type I isotherm observed in the 1M, 3M, and 6M samples. Together with the isotherm analysis, the determination of pore size further confirmed the changed towards mesoporosity. The pore size in the 9M sample increased to 14.10 nm, while the 12M sample rose to 12.40 nm.

The observed transition from microporous to mesoporous structures in the 9M and 12M samples highlighted the sensitivity of the material's properties to variations in the synthesis solution's molarity.

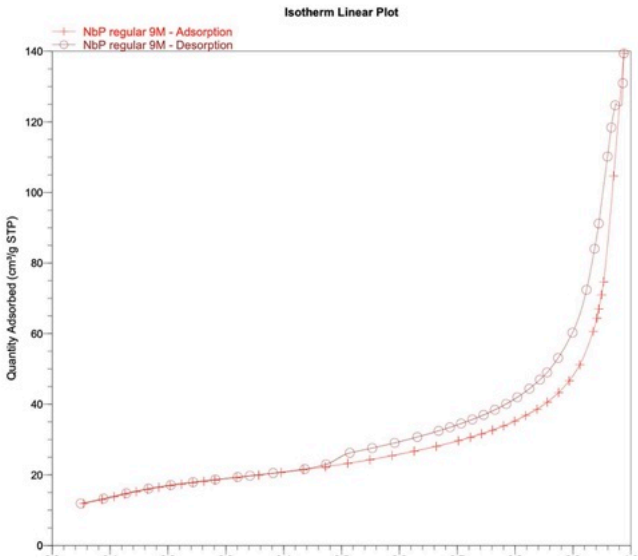

Figure 3.4– NbP 9M adsorption-desorption isotherm

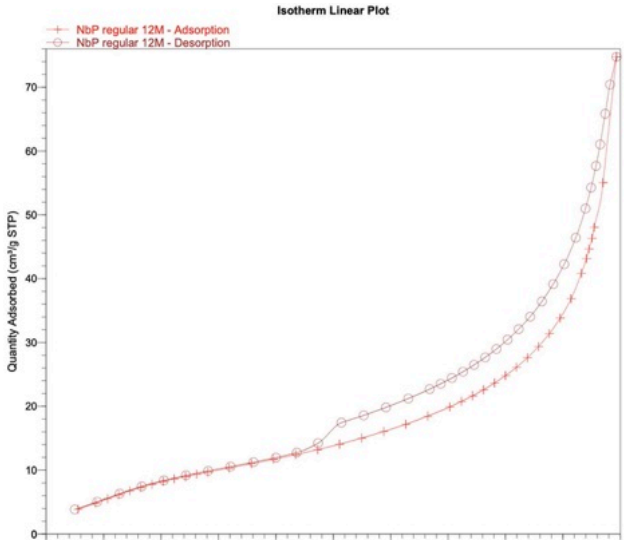

Figure 3.5– NbP 12M adsorption-desorption isotherm

The increase in acidity of the synthesis solution of the catalyst had an impact on its surface area. As acidity increased, there was a decrease in the surface area of the catalyst, going from an average value of more than 200m^2/g in the 1M, 3M, 6M cases to 61m^2/g for the 9M and 37m^2/g for the 12M.
A summary of the different properties revealed by the BET analysis are summed up in the *Table 3.1* below:

Sample	Surface area [m^2/g]	Pore diameter [nm]	Pore volume [cm^3/g]	Category
1M	289.83	2.6	0.18	Microporous
3M	250.27	2.7	0.15	Microporous
6M	189.49	3.08	0.14	Microporous
9M	61.10	14.10	0.21	Mesoporous
12M	37.32	12.40	0.11	Mesoporous

Table 3.1– $NbOPO_4$ characteristics at different molarities

3.1.2.2 TPD[29,30]

TPD gave information about the transition from Lewis to Brønsted acid sites. This transition corresponded to an increase in the solution's acidity during the catalyst synthesis process.
Figure 3.6 provides a visual representation, using distinct colors for Lewis and Brønsted acid sites. Peaks at different temperatures gave information about the prevalence of acid sites within the compound. Accordingly, the left peak, occurring around 210°C, showed the presence of Lewis acid sites while the peak at around 375°C corresponded to the presence of Brønsted acid sites. In the 9M and 12M samples, this peak shifted to the right, entering the Brønsted acid sites region. This shift suggested a more balanced distribution between the two types of acid sites.
This observation provided valuable insights into the catalyst's expected performance, indicating a desirable equilibrium between Brønsted and Lewis acid functionalities.
As the temperature increased, structural decomposition occured around 500°C, marked by a small peak in the graph.

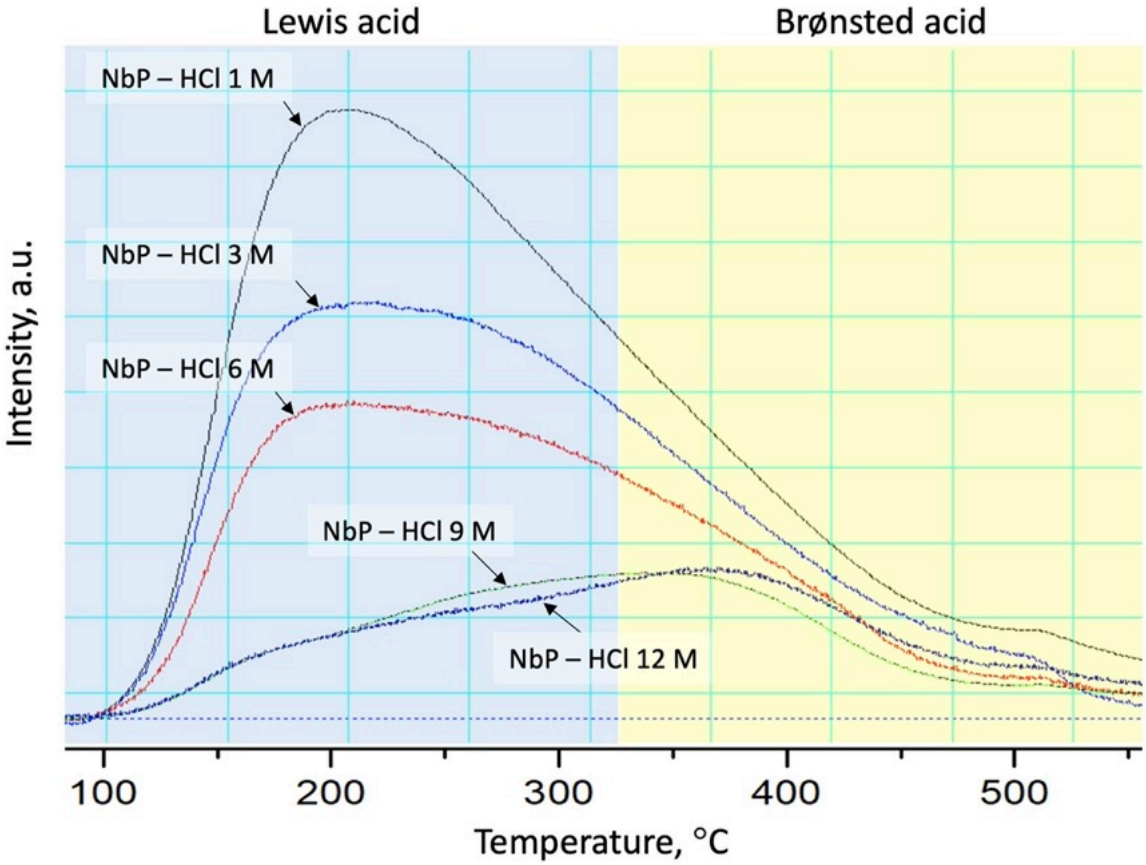

Figure 3.6– $NbOPO_4$ Temperature Programmed Desorption curves at different molarities

3.1.2.3 FT-IR[31]

Analyzing the FT-IR spectra, a contrast is again shown between catalysts synthesized at different molarities of the solution. The different peaks and structure of the synthesized material are shown in *Figure 3.7*. The peak correspondence is retrieved from [31].

The 9M and 12M samples have a defined crystalline structure, where individual compound peaks are present and highly visible and detailed.

In contrast, the 1M, 3M, and 6M samples present a different behavior, presenting an amorphous structure. In these cases, the FT-IR spectra does not have clear peaks, with only slight curves observable in specific wavelength regions of O-Nb-O and PO_4^{3-}.

This distinction in crystallinity observed across different molarities highlights the impact that synthesis conditions have on the catalyst's structural properties.

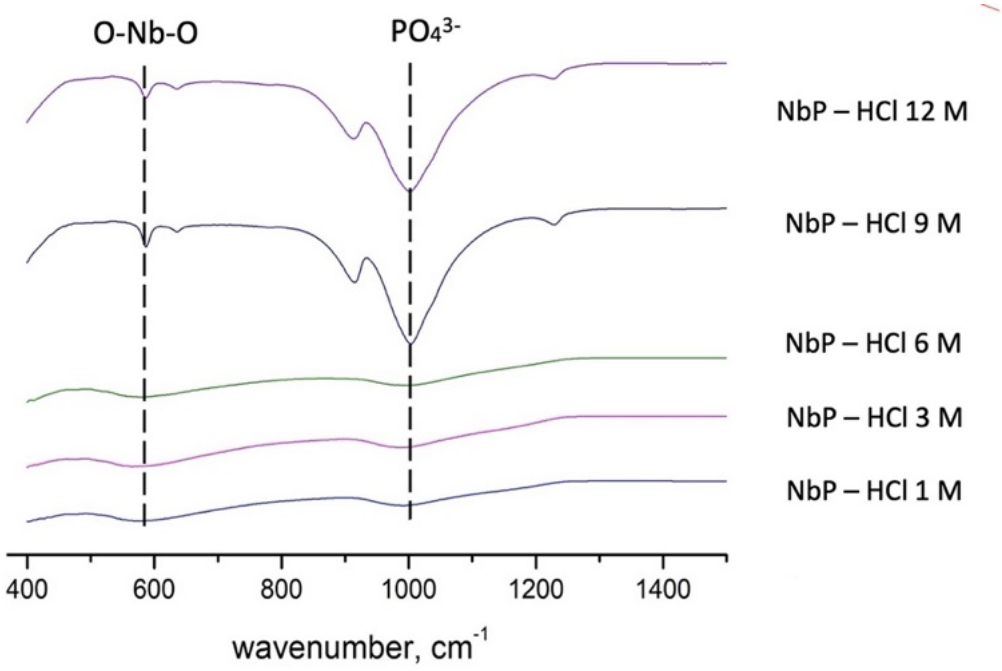

Figure 3.7– $NbOPO_4$ FT-IR diagrams

3.1.2.4 XRD[32]

The XRD patterns gave information about the material's atomic arrangement, revealing a clear difference between the crystalline and the amorphous phases as already observed in the FT-IR diagrams. Also in this analysis the 9M and 12M samples presented a crystalline structure confirmed by clear peaks on the diagram, while the 1M, 3M, and 6M samples have an absence of defined peaks, confirming their amorphous phase.

The use of [32] allowed to confirm the presence of all the NbP bonds inside the materials comparing the peaks present in the *Figure 3.8*.

The contrast in XRD diagrams among different molarities allowed to confirm the development of a different structure with the variations in synthesis conditions.

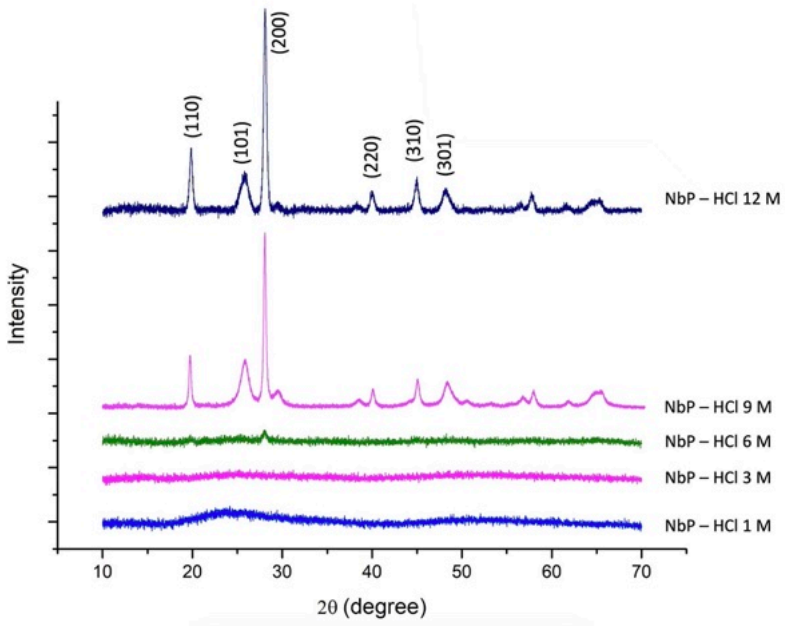

Figure 3.8– $NbOPO_4$ XRD diffractogram at different molarities

3.1.2.5 SEM-EDS

SEM-EDS provided data on the distribution of particles and the elemental composition. It gave a detailed view of how changes in acidity during synthesis can affect the final structure.

Analyzing SEM images revealed a uniform distribution of particles in the structure. Additionally, EDS highlighted compositional changes due to the different acidity synthesis conditions. In highly acidic catalysts, the atomic percentage ratio between P and Nb is 1 to 1. On the other hand, less acidic catalysts show a different stoichiometry, with the ratio between phosphate and niobium atoms being 1 to 2.

This indicates that as acidity increases, there is a proportional increase in the integration of phosphorus into the catalyst structure.

This observation aligns with previous characterizations, providing a consistent validation of the anticipated impact of acidity on the synthesis composition.

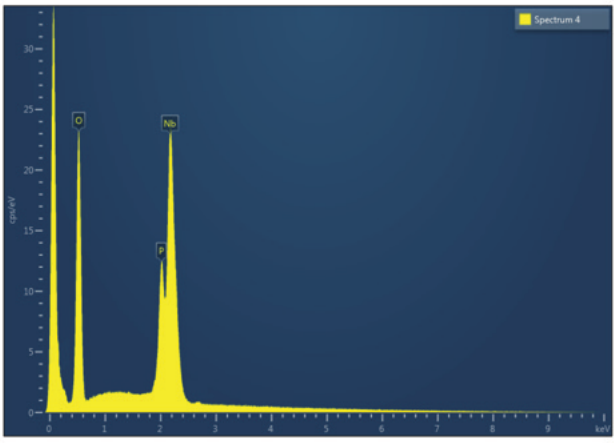

Figure 3.9– $NbOPO_4$ 1M EDS atoms percentage distribution

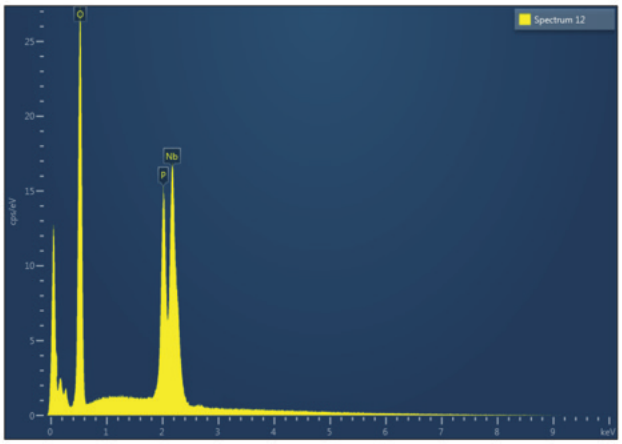

Figure 3.10– $NbOPO_4$ 12M EDS atoms percentage distribution

Element	Atomic %
O	70,17
P	10,81
Nb	19,02

Table 3.2– $NbOPO_4$ 1M XRD atoms percentage distribution

Element	Atomic %
O	71,70
P	14,00
Nb	14,30

Table 3.3– $NbOPO_4$ 12M XRD atoms percentage distribution

SEM-EDS was used to map various materials and explore how atoms are distributed around the material's particles. The results showed the spatial arrangement of Nb, P and O within the catalyst structure. Analyzing the maps allowed to state that the synthesis process is consistent and effective: there is uniformity of Nb, P, and O atoms across the catalyst particles. Two examples (1M and 12M) are reported in *Figure 3.11* and *Figure 3.12*.

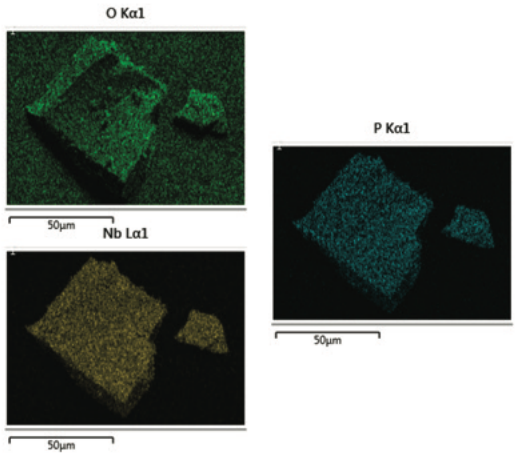

Figure 3.11– $NbOPO_4$ 1M mapping

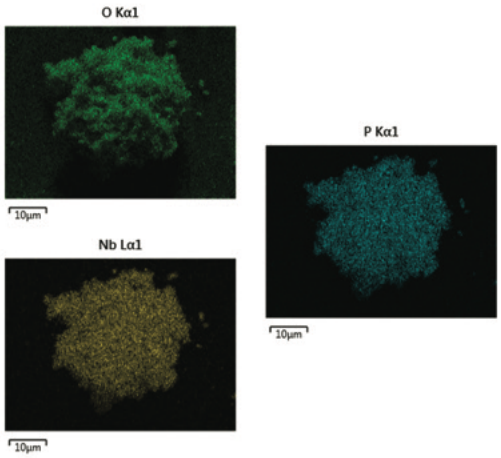

Figure 3.12– $NbOPO_4$ 12M mapping

The evolution from an amorphous to a crystalline phase within $NbOPO_4$ structure became clear in the SEM images, accordingly with the previous data. This transition is observed with the progress from lower to higher molarities, going from 1M and 3M to 6M compounds to the 9M and 12M ones.

In the SEM images of the 1M, 3M, and 6M NbP, a clear absence of crystalline foil is shown, which reveals an amorphous structure. This amorphous phase can be seen in *Figure 3.13*, *Figure 3.14* and *Figure 3.15.*

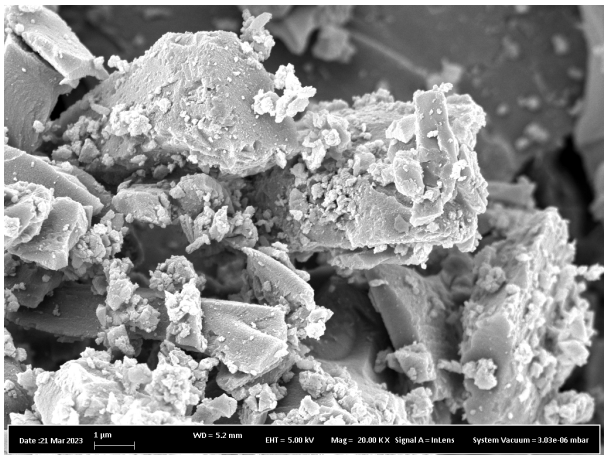

Figure 3.13– $NbOPO_4$ 1M SEM image

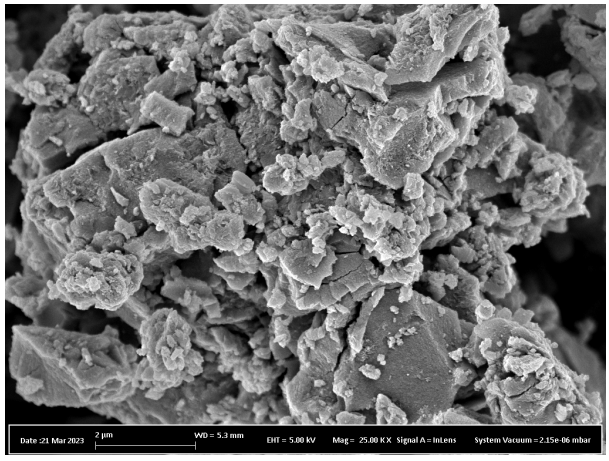

Figure 3.14– $NbOPO_4$ 3M SEM image

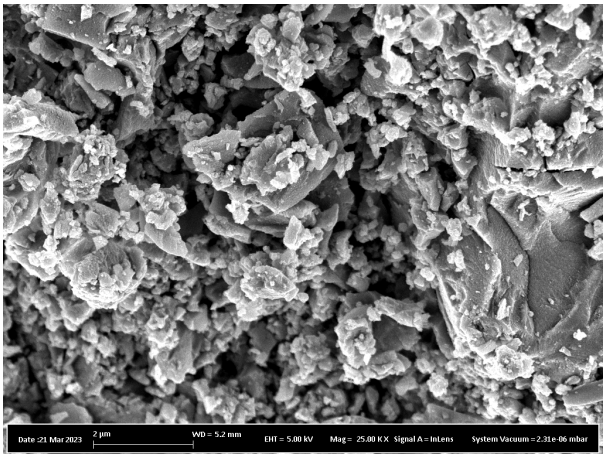

Figure 3.15– $NbOPO_4$ 6M SEM image

On the other hand, the SEM images of the 9M and 12M precursor, as it can be seen in *Figure 3.16* and *Figure 3.17*, present some differences from the amorphous structures observed in the lower molarities. Crystalline foils can be clearly seen in the images, showing defined structure.

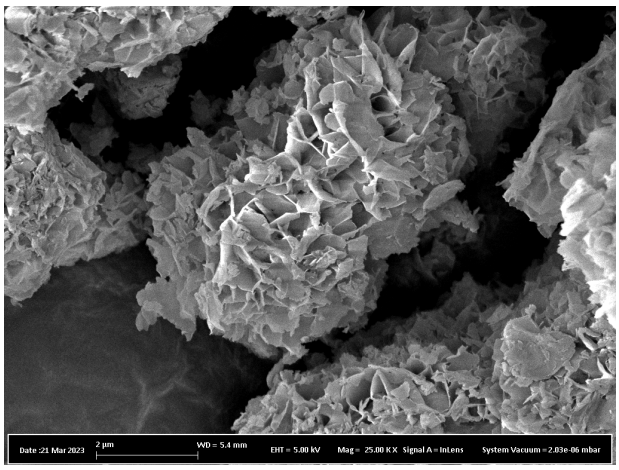

Figure 3.16– $NbOPO_4$ 9M SEM image

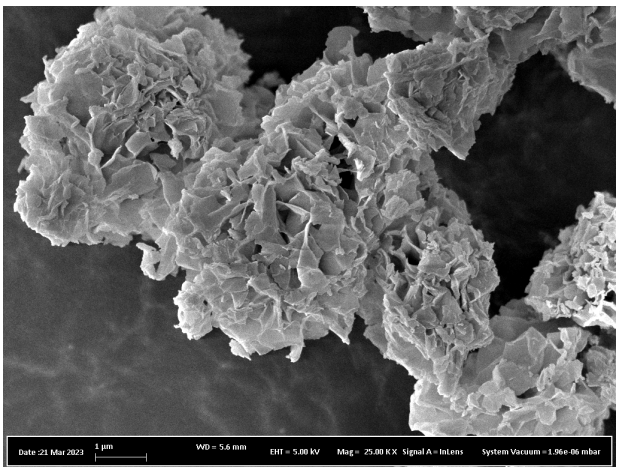

Figure 3.17– $NbOPO_4$ 12M SEM image

Following the analysis of $NbOPO_4$, the following step in the research was to synthesize a support material. This involved the production of a material with properties such as high surface area, to ensure an efficient doping, stability towards acidic conditions, low toxicity, and compatibility with a variety of catalytic applications.

For these reasons the emphasis was placed on developing a TiO_2 support with a high surface area (> 60 m^2/g) and mesoporous structure.

3.1.3 Preparation of TiO_2 support[33-35]

The mesoporous TiO_2 material was synthesized according to different procedures. The synthesis process involved the utilization of a 1-liter HDPE container for the preparation of this material.

The initial step consisted in the mixing of 24.5mL of concentrated 37% hydrochloric acid with 380mL of absolute ethanol within the HDPE container.

To this solvent mixture, a measured quantity of 10g of P123 was added. The resulting solution was then vigorously stirred, maintaining a temperature of 40°C for a period of three hours. This step ensured the complete dissolution and uniform dispersion of P123 within the solution.

Following this step, titanium isopropoxide (TIPO) was added to the solution. The solution was stirred maintaining the temperature at 40°C for an extended duration of 20 hours.

After the 20-hour stirring, a drying process on the solution was carried out.

At this point of the synthesis, different techniques have been utilized.

The first technique involved drying for either 24 or 72 hours, employing two distinct temperatures of 85°C and 95°C. Following the drying phase, a filtration step was implemented, utilizing both vacuum filtration and rotary evaporation. This approach was adopted to ensure the removal of hydrochloric acid. To complete the procedure, a centrifugation process was employed to efficiently recover all the material.

For the second technique, the drying was conducted at a controlled temperature of 35°C while maintaining the relative humidity within the range of 30-50%. This drying phase was sustained for a duration of about seven days, ensuring the removal of solvent and water content from the resultant material. The extended time and the range of humidity were essential for the formation of a mesoporous material, needed for the further step. To guarantee the drying of the catalyst, an additional step was needed. An oven-drying process at a temperature of 95°C for a duration of 24 hours was applied to the material.

The final stage in the synthesis process involved calcination. It was applied in the same manner for all the synthesized materials. Calcination was carried out at a temperature of 500°C, and the process was sustained for five hours. During this phase, the oven was consistently supplied with a controlled air flow, at a rate of 100 liters per hour. This calcination process ensured the complete removal of the organic template from the mesoporous TiO_2 material.

3.1.4 Characterization of TiO_2 support

The different supports obtained with the various techniques were analyzed through BET analysis. All the results are listed in *Table 3.4*.

The choice of the support was based on the combination of high surface area, a mesoporous structure, and a high yield from the synthesis reaction.

After the analysis of the different samples, the support with the best characteristics for the purpose of the study was the one produced using the second technique described in *Section 3.1.3*. This material had sufficiently high surface area (>80 m^2/g), a mesoporous structure, and a good yield in the synthesis reaction (>80%) as highlighted in green in the *Table 3.4*.

Sample n°	Name	Surface area [m^2/g]	Pore diameter [nm]	Pore volume [cm^3/g]	Synthesis reaction yield [%]
1	TiO2 – HCl 12 M – 40C – humidity 50% - 7 days - 500C	85.160	17.259	0.367	81.110
2	TiO2 – HCl 12 M – 85C – 24 hrs – EtOH:H2O 9:1 – 24 hrs – 500C	102.100	12.592	0.322	6.010
3	TiO2 – HCl 12 M – 95C – 24 hrs – 500C	53.130	9.164	0.122	4.060
4	TiO2 – HCl 12 M – 95C – 72 hrs – 500C	56.490	7.575	0.107	77.000
5	TiO2 – HCl 2 to 0.5 M – 85C – 24 hrs – 500C	29.274	15.913	0.116	39.880
6	TiO2 – HCl 2 to 0.5 M – 95C – 24 hrs – 500C	23.606	29.408	0.174	11.700
7	TiO2 – HCl 1 M – 85C – 24 hrs – 500C	39.913	27.541	0.275	42.650
8	TiO2 – HCl 0.5 M – 85C – 24 hrs – 500C	39.565	23.392	0.231	31.320

Table 3.4– TiO_2 supports characteristics

The BET adsorption-desorption isotherm confirmed the mesoporous nature of the support, showing a Type IV pattern. This pattern indicates a well-defined network of mesopores, confirming that the support has the desired structural characteristics.

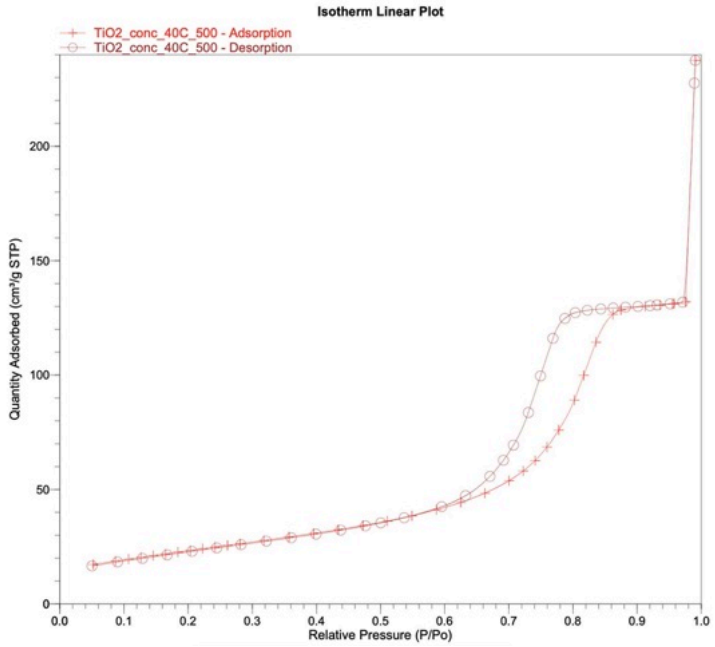

Figure 3.18– TiO_2 BET adsorption desorption isotherm

Creating mesoporous TiO_2 material was a good achievement for this research.
The mesoporous structure was an advantage: it provided a larger active surface area compared to non-mesoporous materials. This increased surface area offered numerous active sites for catalyzing reactions and effectively hosting dopant materials, making the support suitable for the doping of $NbOPO_4$.

3.1.5 Preparation of Ru/$NbOPO_4$/TiO_2 catalyst

3.1.5.1 TiO_2 doping with $NbOPO_4$.

The initial phase of the final catalyst synthesis process involved the doping of mesoporous TiO_2 with NbP, resulting in the production of a material consisted of 20% $NbOPO_4$ and 80% TiO_2. This procedure was carried out using various concentrations of HCl, specifically 1M, 3M, 6M, 9M, and 12M.

To start this preparation, 2g of TiO_2 were introduced into a solution of 50mL of HCl. Then, 0.663g of $NbCl_5$ were added to the TiO_2-HCl solution. The mixture of these components started a reaction that was rigorously stirred for a duration of two hours under ambient room temperature conditions.

At the same time, 0.5645g of $NH_4H_2PO_4$ were added to a separate 50cL HDPE bottle, which contained 50mL of HCl solution, all under the same room temperature conditions. As $NH_4H_2PO_4$ dissolved completely, it was poured into the first solution, forming a homogenous solution. This solution was stirred overnight at a temperature of 80°C.

Following the stirring period, the solution was allowed to crystallize at a steady 80°C for an additional three hours, after which it was cooled down for a duration of two hours. This process facilitated the formation of the desired material characteristics.

The subsequent step involved the separation of the synthesized material from the solution through a vacuum filtration process with deionized water to eliminate any residual impurities.

Afterwards, it was subjected to a drying phase. The drying process was performed at a controlled temperature of 95°C, allowing the material to remove water molecules completely overnight. This ensured the removal of any remaining moisture content.

The final stage in the synthesis was the calcination process, conducted at a temperature of 450°C for a continuous duration of five hours. This phase was needed to guarantee the complete removal of the organic template from the composite material.

3.1.5.2 Ru decoration

Once the $NbOPO_4$/TiO_2 material was obtained, ruthenium (Ru) decoration was performed. To initiate this process, 0.0513g of $RuCl_3$ were dissolved into a solution of 20mL of water. Subsequently, 0.975g of the $NbOPO_4$/TiO_2 material were incorporated into this solution.

The solution was vigorously stirred overnight to ensure the uniform deposition of Ru onto the composite material. To complete this phase, the solution was dried in an oil bath for one and a half hours, followed by overnight drying in an oven at 110°C to guarantee thorough desiccation.

The synthesis process finished with the reduction step, which was conducted for six hours under a continuous flow of hydrogen gas at a rate of 50 mL per minute, all at a controlled temperature

of 400°C. This final step aimed to remove water molecules still present in the final powder to optimize the material's properties.

3.1.6 Characterization of $NbOPO_4/TiO_2$ intermediate

The main characterization techniques utilized for the intermediate involved analysis using XRD and SEM-EDS. These techniques were selected to check the crystallinity, evaluate the presence of $NbOPO_4$ within the structure, and determine the homogeneity of catalyst distribution.

3.1.6.1 XRD

In the examination of the NbP-TiO_2 loaded catalyst, the first analysis was conducted using XRD. The patterns revealed the crystalline structure of TiO_2 with defined peaks and the presence of NbP was given by the distinct peak attributed to it observed in the 9M sample in *Figure 3.19*. This confirmed the successful doping of NbP onto the TiO_2 support.
Furthermore, additional information was obtained comparing the $NbOPO_4$/TiO2 structures with the NbP structure. In the XRD diagrams of the materials prepared with lower HCl concentration, namely the 3M and 6M, the peak corresponding to Nb was not evident, confirming their amorphous nature.
In summary the XRD results confirmed the crystalline nature of TiO_2 and validated the effective doping of NbP, especially noticeable in the 9M sample.

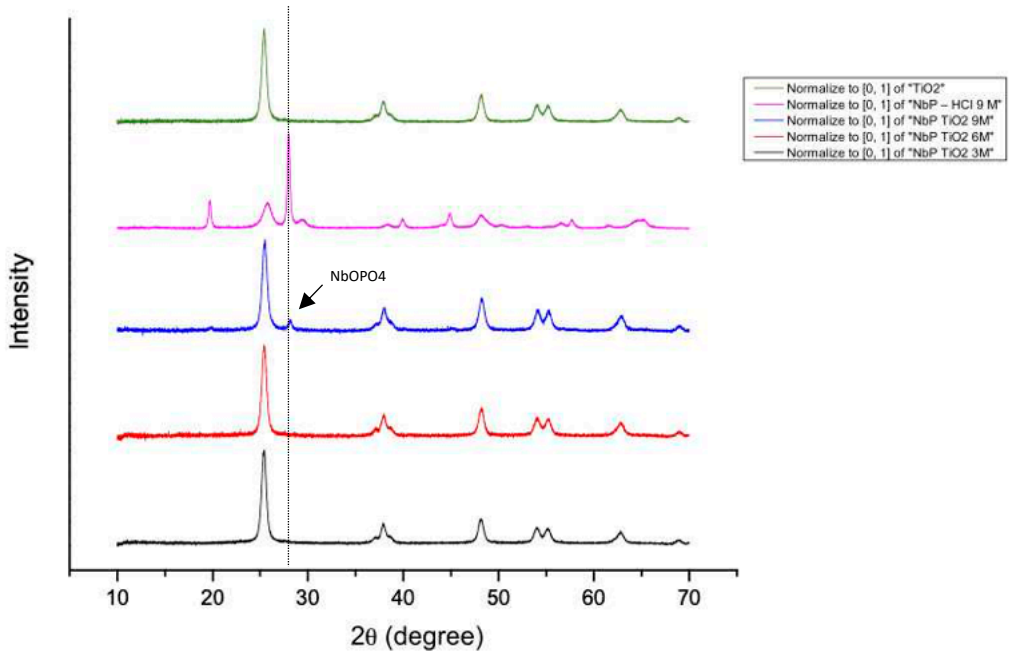

Figure 3.19– XRD diagrams of NbP-TiO_2

3.1.6.2 SEM-EDS

SEM-EDS analysis on the 9M $NbOPO_4/TiO_2$ sample provided information about the structural modifications of TiO_2 induced by NbP doping. Interestingly, the SEM-imaging revealed the presence of NbP crystalline "sheets" overlaying TiO_2, as it can be seen in *Figure 3.20*.
This result confirmed the successful doping process. Besides, the sheet structures formed by NbP highlighted specific interactions with the catalyst matrix, which could be helpful for the catalyst activity.
Overall, the SEM-EDS analysis strengthened our understanding of NbP and TiO_2 interaction and assessed the efficiency of the doping technic.

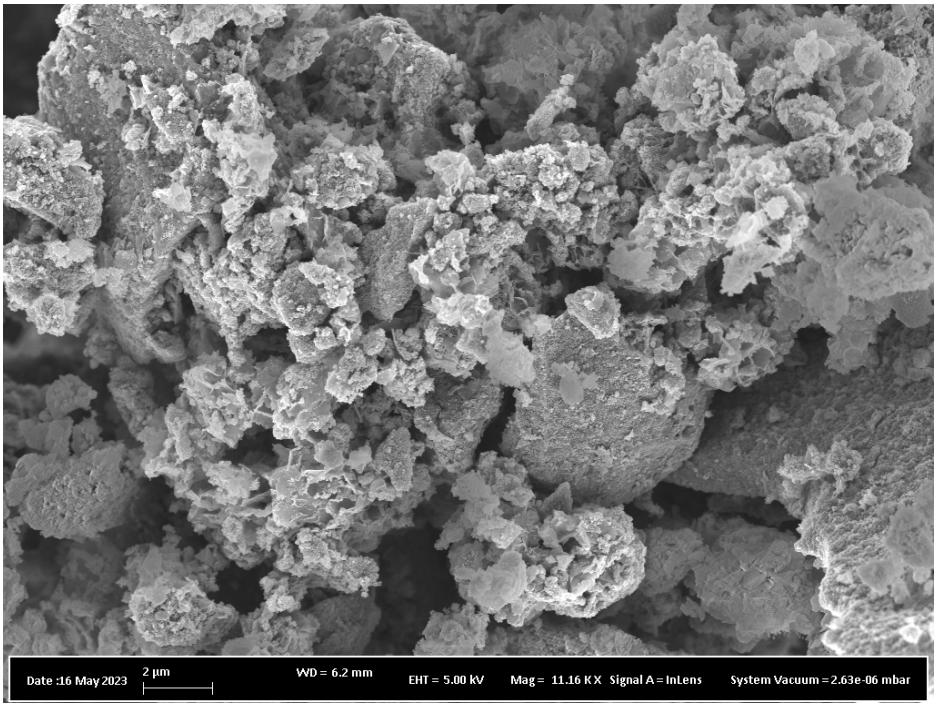

Figure 3.20– $NbOPO_4/TiO_2$ SEM image

3.1.7 Characterization of $Ru/NbOPO_4/TiO_2$ catalyst

The only analysis done to the final catalyst was TEM and EDX

3.1.7.1 TEM

TEM analysis was performed on $Ru/NbOPO_4/TiO2$ catalyst to assess the Ru particles' distribution across the catalyst structure. In fact, Ru distribution is a good indicator of the efficiency of the decoration process, which is important to reach higher catalytic performance. *Figure 3.21* obtained by TEM showed a homogenous distribution of Ru particles on the catalyst. This observation not only confirms the successful decoration process, but also provides interesting information on the size and the dispersion features of Ru particles.
Besides, quantification of particles size revealed an average diameter of 2nm.
The small particle size increases the area to volume ratio, and therefore provides a higher number of active sites for the reaction.

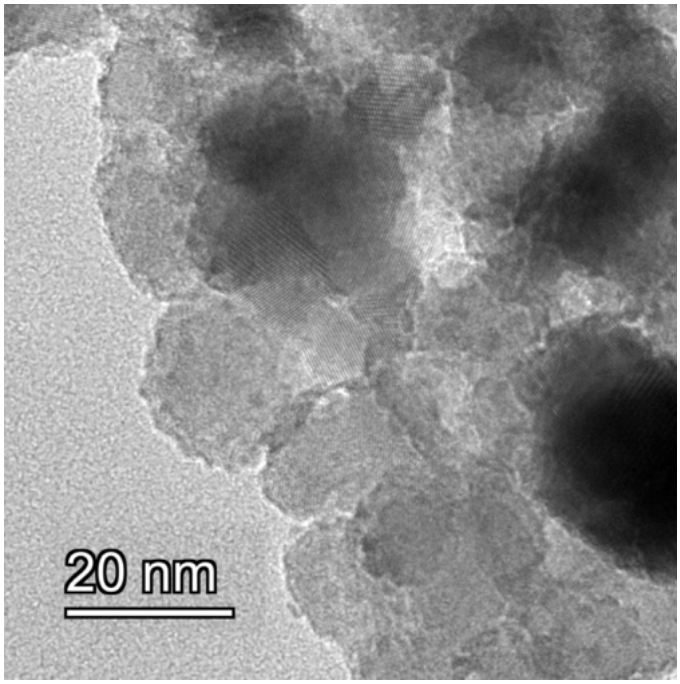

Figure 3.21– Ru particles on $NbOPO_4/TiO_2$ structure

3.1.7.2 EDS

EDS mapping gave information about the particles' distribution over the final catalyst. It can be seen from *Figure 3.22* which represent the 9M sample of the final catalyst.
This detailed distribution is important to ensure that each atom is homogeneously present in the material to maximize the active surface area of the catalyst.

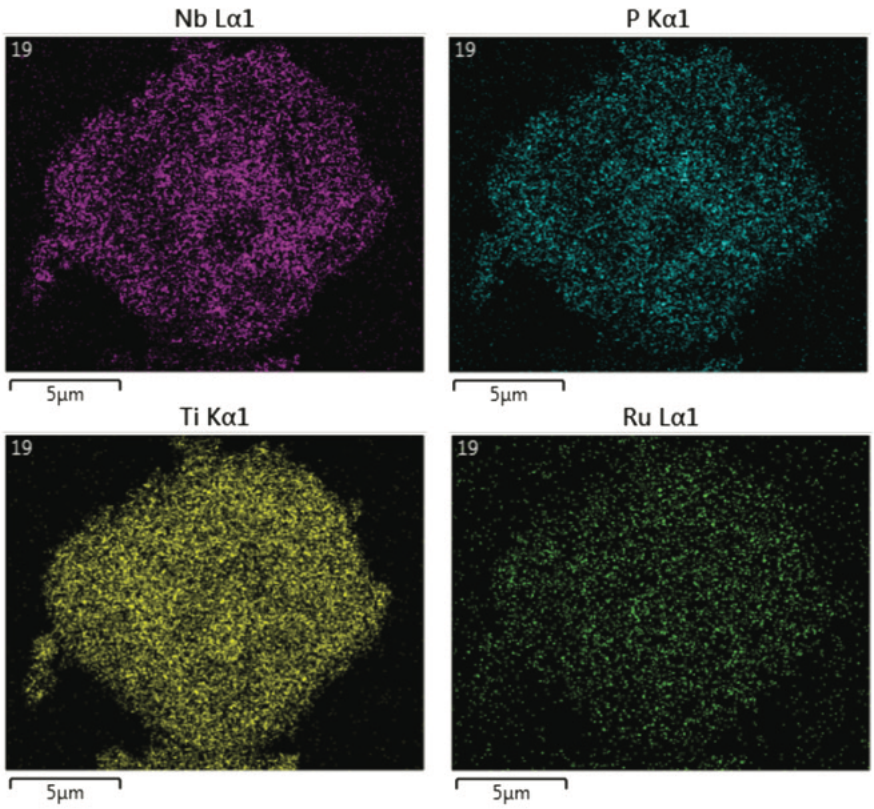

Figure 3.22 – Atoms distribution in $Ru/NbOPO_4/TiO_2$ catalyst

In conclusion, the characterization of the final catalyst has revealed promising results, allowing further analysis in hydrodeoxygenation reactions under varied conditions. The particle distribution is homogeneous, and the catalyst exhibits a consistent structure. Based on the obtained data, the decision was made to advance the study by examining the reaction using catalysts prepared with all the different molarities of HCl solutions. This approach aims to comprehensively understand the activity of each distinct catalyst in the hydrodeoxygenation process.

Chapter 4
Catalytic activity and kinetics study

This chapter covers the last three aspects of the project: the hydrogenation reaction setup, the catalytic activity, and a preliminary kinetic study. Firstly, the elements of the reaction setup, including the reactor, temperature control, reaction conditions, and the techniques used to analyze the products are described. In the section on catalytic activity, it explores the effects on the products of different temperature and reaction time conditions along with the different acidity synthesis conditions of the catalyst. Finally, the result of a preliminary kinetic study is presented, which focused on understanding the reaction rate.

4.1 Reaction setup

4.1.1 Instrumentation setup

In the experimental setup reactions were carried out in an autoclave through a batch process. The autoclave was sealed to prevent any external influence from interfering with the reaction inside and to promote accuracy in the experimental results. An autoclave with a volumetric capacity of approximately 15mL was chosen to adapt to the specific requirements of the experimental procedure.

A magnetic stirrer was integrated into the autoclave setup to ensure homogeneity within the reaction mixture and the highest surface area contact of the catalyst with the reactant.

Safety considerations were taken in the design of the autoclave system to mitigate potential risks associated with high-pressure conditions. A pressure gauge was integrated into the autoclave design to constantly monitor and display the internal pressure. This pressure monitoring allowed to track the progress of the reaction and address any deviations from the pressure range. In case of unexpected issues or a too high pressures, an emergency relief valve was placed to ensure a controlled release of pressure, preventing any potential incident.

Furthermore, the reactor was heated through an external metallic jacket connected to a digital temperature controller. The controller was integrated into the autoclave system to maintain control over the reaction temperature. This allowed to set and regulate the desired temperature

conditions with a high degree of precision and accuracy, contributing to the reliability of the experimental results. A scheme of the overall setup can be observed in *Figure 4.1*.

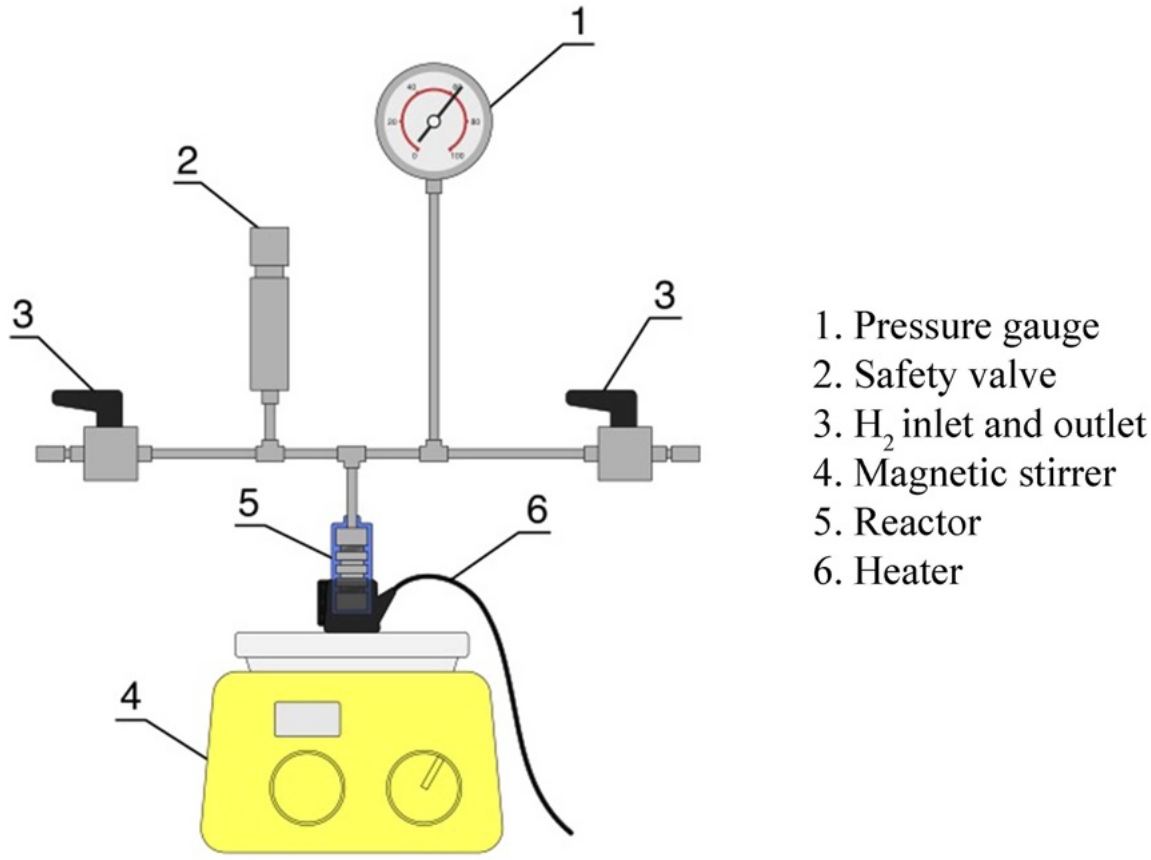

Figure 4.1– Reaction setup

4.1.2 Reaction conditions[14]

The aim of this experiment was to achieve a complete conversion of eugenol into non-oxygenated hydrocarbons. In the initial phase of the reaction setup, a measured quantity of 50mg of catalyst, 187µL (approximately 200mg) of eugenol, and 5mL of cyclohexane, used as solvent, were loaded into the autoclave. Then, the autoclave was subjected to a purging process where hydrogen gas (99.99% purity) was introduced multiple times to displace any residual air within the system. Following this purging, the autoclave was pressurized to obtain the desired hydrogen pressure, which was set at 50 bars.

The core of the experiment involved heating the reaction mixture to a temperature range of 175 to 225 °C, maintained for a duration of 4 to 12 hours, during which vigorous stirring was applied.

After the set reaction time was reached, the autoclave was cooled down to room temperature. Subsequently, the pressure of the hydrogen gas was released. To assess the success of the reaction and determine the composition of the resultant product, a sample of 1000 µL was collected. The collected sample was analyzed using Gas Chromatography with Flame Ionization Detection (GC-FID) and Gas Chromatography-Mass Spectrometry (GC-MS) techniques.

4.1.3 Products analysis techniques

4.1.3.1 Gas chromatography – Flame Ionization Detector[36,37]

Gas chromatography (GC) is a technique utilized in analytical chemistry to separate and analyze volatile compounds within a mixture. The fundamental principle involves the separation of a mixture into its individual components based on their respective affinities for a stationary phase and a mobile phase.

In Gas Chromatography with Flame Ionization Detection (GC-FID) gas chromatography separates individual components of a sample, and flame ionization detection measures the concentration of these separated compounds.

The operation of GC-FID involves several key steps. First, in the Gas Chromatography (GC) step, the sample is vaporized and introduced into a chromatograph. It is then carried by an inert gas through a chromatographic column. This column separates the individual components based on their affinities for the stationary phase.

As the separated compounds are extracted from the gas chromatograph, they pass through a hydrogen-air flame in the Flame Ionization Detection (FID) step. The FID detector consists of a hydrogen flame and a collector electrode. When organic compounds in the sample pass through the flame, they are ionized, generating positively charged ions and electrons.

The positively charged ions produced in the flame are collected at the collector electrode, resulting in an electrical current. The magnitude of this current is directly proportional to the concentration of the compounds passing through the flame.

The electrical current generated is then converted into a signal, which is recorded as a chromatogram. The peaks in the chromatogram correspond to the different compounds present in the sample. The area under each peak is proportional to the amount of the corresponding compound, allowing for quantification.

The Flame Ionization Detector (FID) is highly favored in gas chromatography due to its near-universal response to organic compounds, low detection limits, long-term stability, simplicity of operation, and a broad linear response range. It provides reliable results for complex mixtures and facilitates direct percent composition reports.

The FID's functionality is based on the combustion of organic compounds in a hydrogen-air flame. The detector's performance is influenced by factors such as carrier gas-to-hydrogen-to-air flow rate ratios and detector geometry. Flame stability sets upper and lower bounds on individual gas flow rates. Generally, operating conditions recommended by the manufacturer are optimal for performance.

The liquid HDO reaction products were identified on an Agilent 7820A GC equipped with an HP-5 MS capillary column (30 m length, 0.25 mm internal diameter, and 1 µm of film thickness) and FID detector.

The GC injection port and the detector temperature were set at 250 °C while the column temperature was ramped from 50 to 250 °C, at a rate of 5 °C/min while Helium was used as the carrier gas. The instrument used in this study can be seen in *Figure 4.2*.

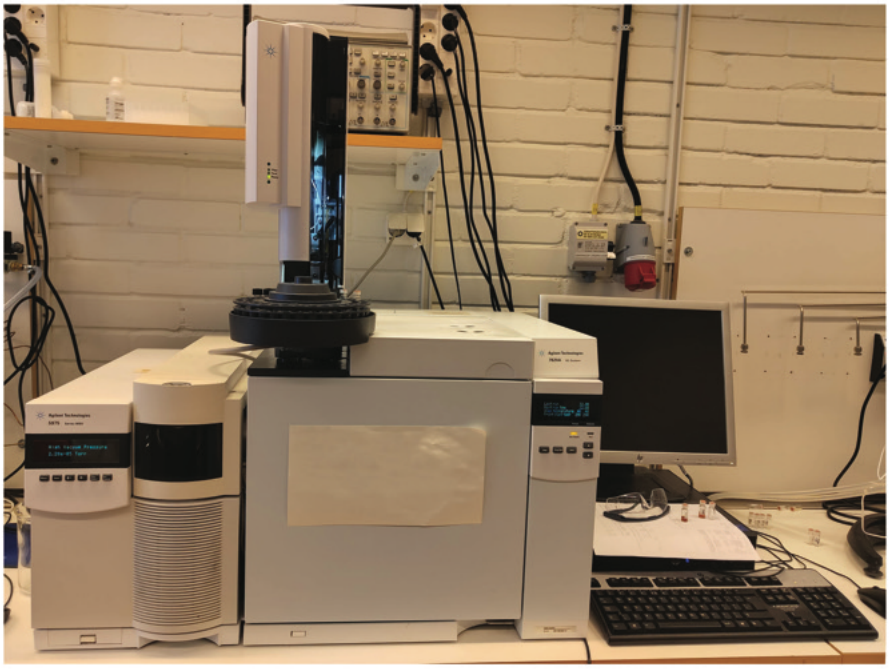

Figure 4.2 – Agilent 7820A GC equipped with an HP-5 MS capillary column and FID detector.

4.1.3.2 Gas chromatography – Mass Spectroscopy[36]

Gas Chromatography-Mass Spectrometry (GC-MS) is a powerful analytical technique that combines the separation capabilities of gas chromatography with the detection and identification capabilities of mass spectrometry.

In GC-MS, samples in liquid, gaseous, or solid form are vaporized and separated using a gas chromatograph. The components are driven by an inert gas through a capillary column, where they are extracted at different times based on their boiling points and polarities. This separation allows for the analysis of complex mixtures with hundreds of compounds.

Once separated, the components are ionized and fragmented by the mass spectrometer. The ions are then accelerated through a mass analyzer, which sorts them based on their mass to charge ratios (m/z). GC-MS can operate in full scan mode, covering a wide range of m/z ratios, or selected ion monitoring (SIM) mode, targeting specific masses of interest.

Different types of analyzers, such as magnetic sector, quadrupole or ion trap, are used to select ions by their molecular weight. The resulting mass spectrum reflects the molecular weight and structure of the sample, making the identification easier through comparison with a library or a previous analysis.

Finally, ion detection and analysis are performed. Fragmented ions appear based on their m/z ratios. The peak areas in the gas chromatogram correspond proportionally to the quantity of the respective compound. GC-MS produces distinctive mass spectra for each peak, enabling the identification and quantification of unknown compounds using libraries and literature of mass spectra.

The quantification of HDO products were based on GC-MS. The analysis was performed in an Agilent 6890 N GC equipped with a HP-5 MS capillary column (30 m length, 0.25 mm internal diameter, 0.25µm film thickness) and a MS detector (Agilent 5579 N), showed in *Figure 4.3*.

The quantification of the eugenol and deoxygenated products were based on calibration curves obtained with commercially available standard compounds (nonane and eugenol).

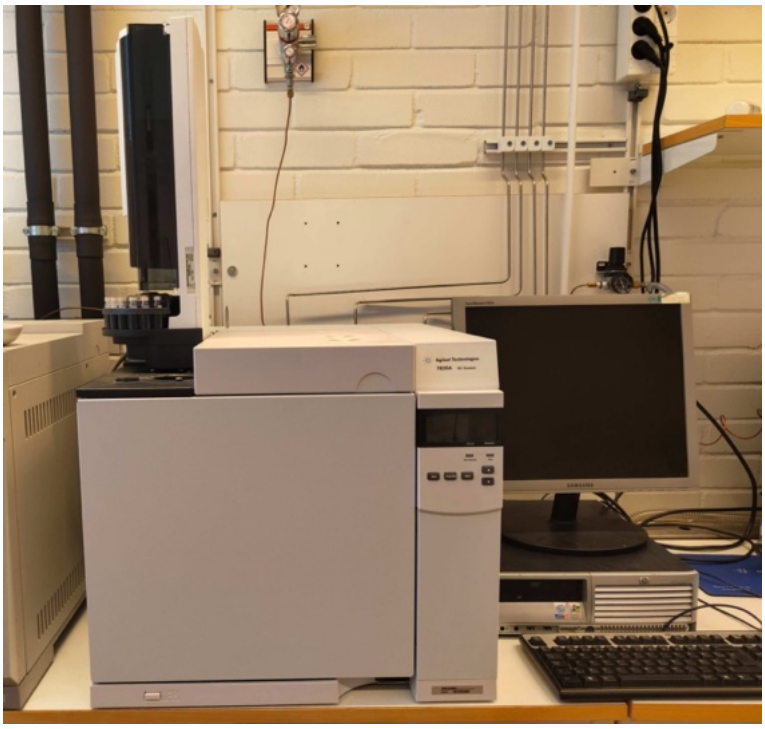

Figure 4.3 – Agilent 6890 N GC equipped a HP-5 MS capillary column and MS detector.

4.2 Catalytic activity

In the experimental analysis, the conversion of eugenol was determined using *Equation 4.1*:

$$Conversion(\%) = \left(\frac{C_0 - C_t}{C_0}\right) \times 100 \quad (4.1)$$

Where C_0 represents the concentration of eugenol at the initial time (0 hours), and C_t represents the concentration of eugenol at a specific time t (hours).

Moreover, the yield of hydrodeoxygenation (HDO) products, specifically the target product (denoted as [4] in *Figure 4.8*) and the total hydrocarbons, were determined from concentrations calculated through peak areas identified by Gas Chromatography-Mass Spectrometry (GC-MS). These concentrations were then compared with the calibration curves established for the previously mentioned compounds (nonane and eugenol).

4.2.1 Temperature effect

The evaluation of catalytic activity was first assessed at different temperatures. Each reaction lasted 12 hours for each $Ru/NbOPO_4/TiO_2$ catalyst. The aim was to identify the temperature at which the catalyst was active.

Initially, a temperature of 225°C was applied to all the catalysts except that which was prepared under 1M HCl. In *Figure 4.4,* it can be seen that all catalysts completely converted, highlighting the catalyst's efficacy.

Moreover, Gas Chromatography (GC) analysis indicated a yield >90% towards the target product and the absence of oxygenated or unsaturated compounds with the resulting hydrocarbons fully hydrogenated.

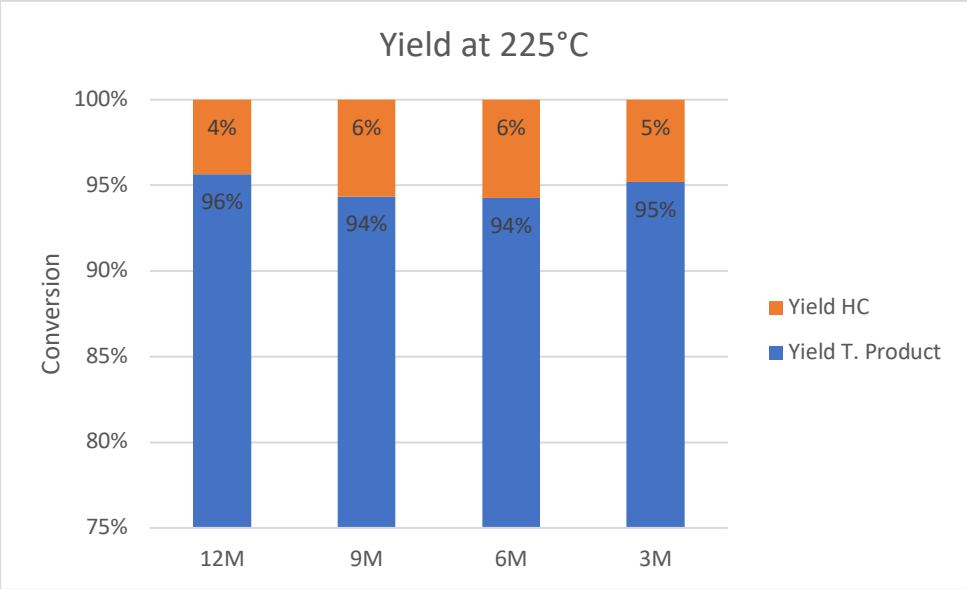

Figure 4.4 – Yield and conversion of eugenol at 225°C

To further explore the catalyst's performance, a subsequent test was conducted at 200°C specifically for the 9M and 3M catalysts. Again, both catalyst concentrations demonstrated full conversion and maintained high selectivity under these conditions.

In the following step, the temperature was reduced to 175°C. At this point, the catalyst's activity decreased significantly. As is shown in *Figure 4.5* that only approximately 40% of the main products were produced, while the remaining compounds consisted of unreacted reagents and oxygenated by-products. This observation indicated that the catalyst was not active under 200°C.

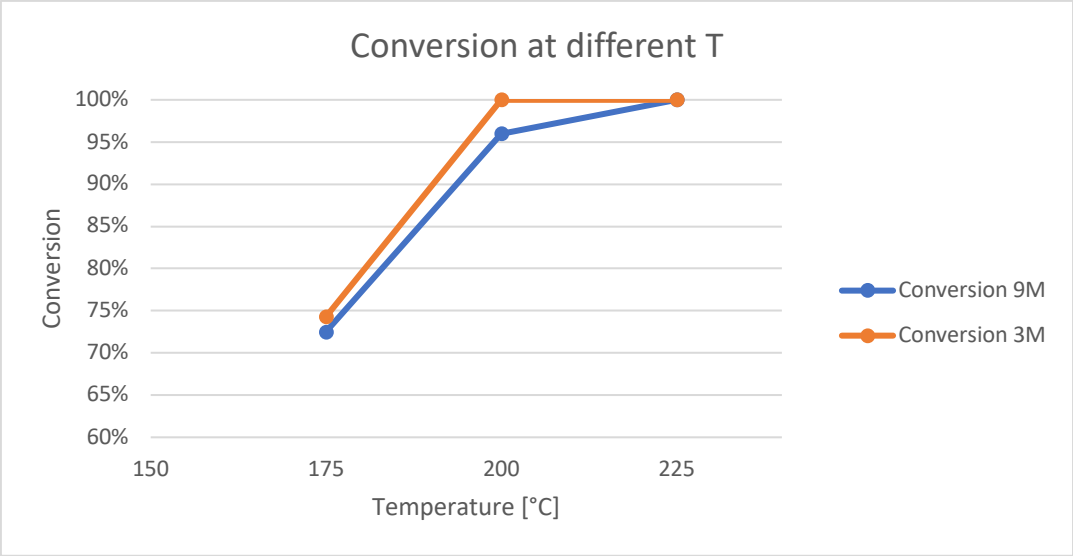

Figure 4.5 – Conversion of eugenol at different temperatures

In summary, the catalyst presented activity at 200°C, a good improvement in comparison to findings from other studies.[9-13]

To understand more about the reaction kinetics and mechanism, further investigations involved conducting reactions at 200°C, over various time intervals. This detailed analysis aimed to construct a primary reaction mechanism and provide information about the catalyst's behavior over time.

4.2.2 Time effect

Following the setting of the best reaction temperature, a study into the influence of reaction time was conducted. Each catalyst was utilized in reactions for 2, 4, 8, and 12 hours at 200°C to understand the conversion at different time and be able to predict a reaction mechanism.

A significant transformation occurred after 8 hours, with conversion greater than 80% achieved for all the catalysts. The results then indicated that after 12 hours the conversion went over 90%, reaching almost 100% for all the catalysts except the 1M.

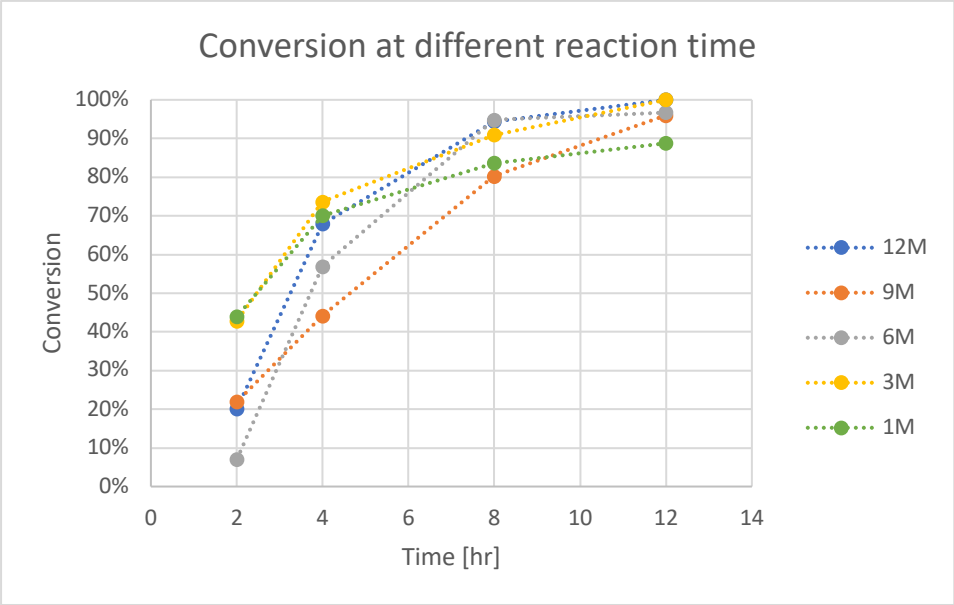

Figure 4.6 – Conversion of eugenol at different time using different catalysts at 200°C

From the data it was seen that the yield between the 2 and 4-hour intervals showed minimal increments. During these stages of the reaction, a high presence of oxygenated products was observed in both cases, indicating a slower progression of conversion, as it can be seen in *Figure 4.7* and *Figure 4.8*.

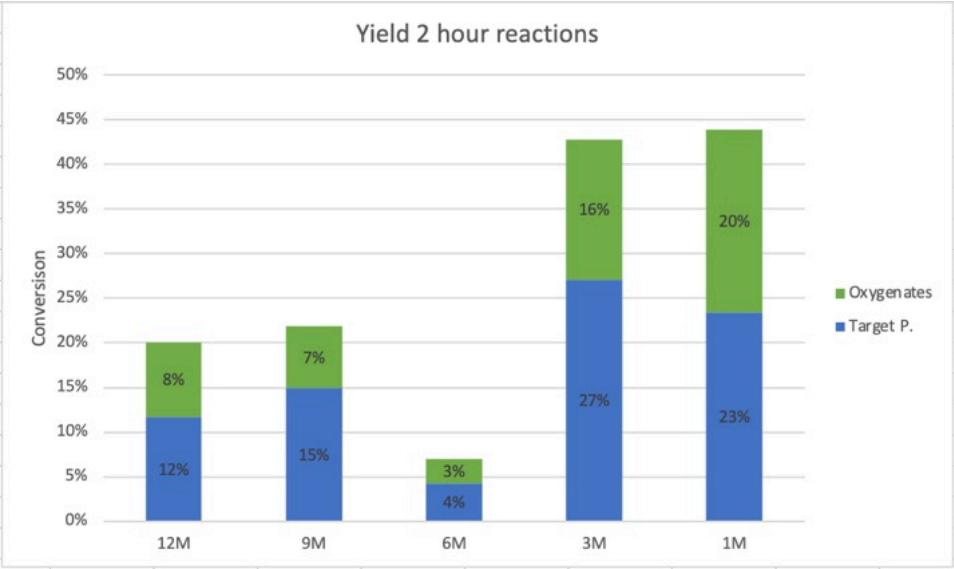

Figure 4.7 – Reaction yield after 2 hours at 200°C

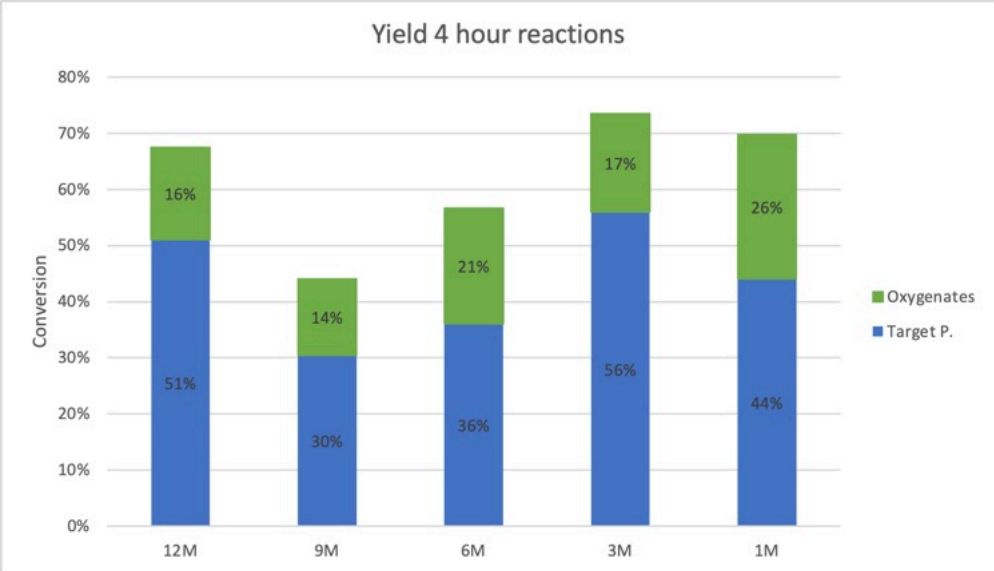

Figure 4.8 – Reaction yield after 4 hours at 200°C

In summary, the time-dependent study revealed that the reaction reached a critical point after 8 hours, achieving good conversion rates. The following increase in conversion from 8 to 12 hours highlighted the importance of a greater reaction times for maximizing the conversion.

4.2.3 Catalyst acidity effect

Considering the high conversion obtained with the different catalysts after 12 hours, an analysis on the products yield between the five catalysts has been carried out to study the differences between them.

It can be noted from the *Figure 4.9* that the 1M catalyst has lower activity, displaying a lower conversion and lower yield compared to the other catalysts. In contrast, the 12M and 3M catalysts demonstrated very high activity and complete yield toward hydrocarbons and target product.

Moreover, the 6M and 9M catalysts showed good activity, reaching conversions greater than 90% and yields greater than 80%.

Overall, the analysis revealed that there was not a clear difference from the 3M to the 12M. It denoted that the change in the acidity of the synthesis solution of the catalyst does not have a great influence on the catalytic activity of the catalyst itself. All the catalyst prepared with molarity greater than 3M showed good catalytic activity. A more detailed study must be carried out to understand which one is the best.

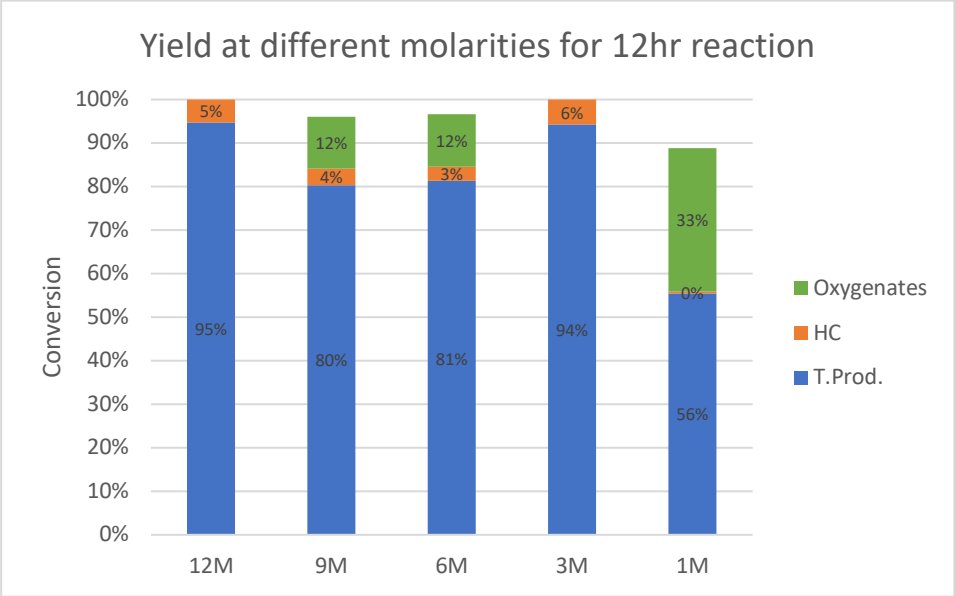

Figure 4.9 – Reaction conversion and yield after 12-hour reactions at 200°C

4.2.4 Reaction mechanism

From the different reaction times studied, a preliminary reaction mechanism was constructed, as illustrated in *Figure 4.10*. The mechanism describes the eugenol conversion steps during the catalytic process.

Initially, the double bond situated on the external carbon of eugenol is saturated.

Subsequently, the ether bond is cleaved, signifying a significant structural modification. The resulting benzene ring is then saturated, eliminating any remaining double bond.

The final stages of the reaction, occurring mainly after 8 and 12 hours, involve the cleavage of the -OH bond and the consequential "opening" of the ring structure. This last step results in the conversion of the target product into smaller hydrocarbons; still considered as good products.

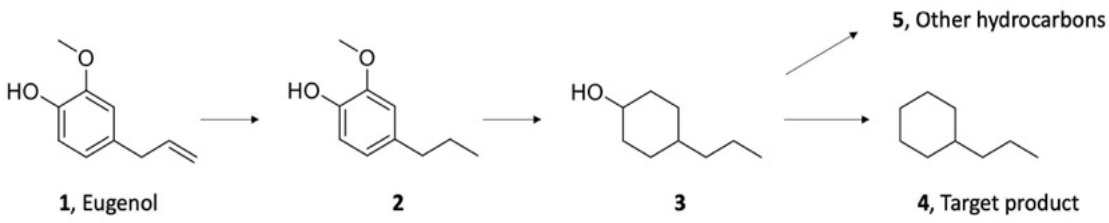

Figure 4.10 – HDO reaction mechanism of eugenol

4.2.5 Comparison with Ru/C and Ru/TiO_2

To assess the catalytic performance of Ru/$NbOPO_4$/TiO_2, comparative studies were conducted using two additional catalysts: Ru/C, utilizing commercial carbon, and Ru/TiO_2. The TiO_2 employed in this study was synthesized in the laboratory, using the same technique applied in the preparation of the catalyst under study. The evaluation involved 12-hour reactions at 200°C for both comparative catalysts.

The data on the conversion and on the yield of the single products are shown in the *Figure 4.11* and in *Table 4.1*.

The results obtained from these comparative studies revealed distinctive differences from the Ru/$NbOPO_4$/TiO_2 catalysts showed in *Figure 4.7*. Both Ru/C and Ru/TiO_2 displayed low yield towards the main product and other hydrocarbons, displaying a significant presence of oxygenated products in the reaction output. Specifically, Ru/C demonstrated a yield only greater than 50%, while Ru/TiO_2 exhibited even lower yield, only slightly greater than 30%.

These data highlighted the important role played by all three components (Ru, NbP, and TiO_2) in the final catalyst. The catalytic system's efficacy in achieving high conversion and yield towards hydrocarbons hinges on the synergistic interaction of these components.

In summary, the comparative analysis elucidates the integral role played by each component in the Ru/$NbOPO_4$/TiO_2 catalyst, confirming its higher performance in achieving high conversion and yield towards hydrocarbons compared to the evaluated alternatives.

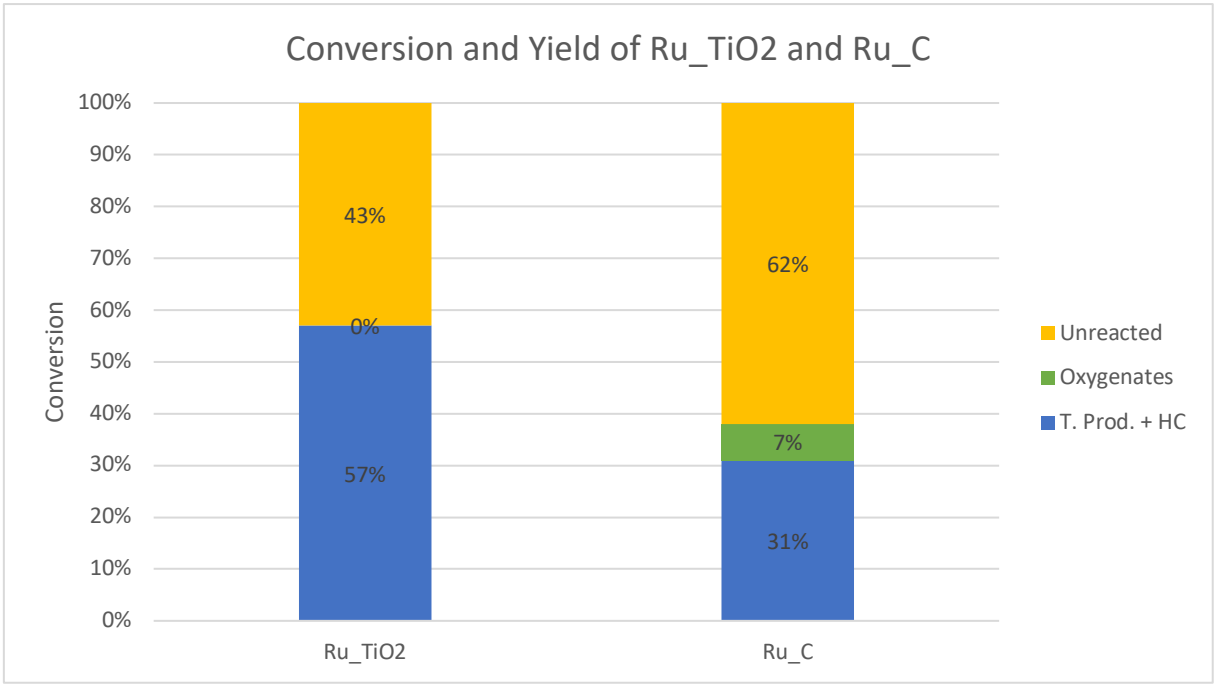

Figure 4.11 – Conversion of eugenol and yield of the products using Ru/TiO_2 and Ru/C for 12-hour reactions at 200°C

Sample	Conversion
Ru_TiO_2	57%
Ru_C	38%

Table 4.1 – Conversion of eugenol using Ru/TiO_2 and Ru/C for a 12-hour reactions at 200°C

4.2.6 General considerations and perspective[10,14,38,39]

Given the results some general considerations about the activity of the catalysts were made. The increase of acidity in the synthesis solution revealed no observable difference in the catalytic activity among the various catalysts, except for the 1M, which showed lower conversion and yield. Catalysts from the 3M to 12M demonstrated consistent activity, as well as high yield of the target product and of the fully saturated hydrocarbons.

The reaction conditions employed in this study presented notable improvements compared to previous research. The catalysts showed activity at a relatively low temperature of 200°C, a considerable reduction from the temperatures traditionally utilized in hydrodeoxygenation reactions, usually much greater than 225°C. Additionally, the pressure conditions were milder, but they still present an opportunity for further optimization.

In conclusion, the comprehensive analysis suggests that each component of the catalyst has an important role to achieve high conversion and yield under milder reaction conditions. Future studies could focus on increasing the reactant-to-catalyst ratio, transitioning from 4:1 to a higher proportion. Furthermore, exploring lower pressure conditions and employing a higher reaction volume could offer additional paths for process optimization.

Additionally, an important aspect of future work involves conducting a reusability test on all the catalysts. This will reveal more on their sustained activity over time and their potential for multiple utilizations. Understanding the catalysts' performance under repeated use is necessary for practical applications and sustainable processes.

4.3 Preliminary kinetic study

A kinetic study is a scientific investigation used to understand the reaction rate of a chemical reaction over time. It involves the measurement and analysis of reaction rates giving information about the factors that influence them, about the determination of reaction mechanisms, and the establishment of mathematical relationships between reactant concentrations and time. The connection of experimental data to reaction rates and mechanisms is achieved through material balances. Given the importance of a specific material balance for each reaction, distinct reactors are characterized by different kinetics study approaches.
In this project, a preliminary kinetic study was conducted for all reactions performed with the various catalysts. The reacting system treated both reactants as if they were processed in a batch reactor.
Assuming the behavior of an ideal batch reactor, the material balance in *Equation 4.2* could be used:

$$\frac{d\underline{c}}{d\tau} = \underline{r}(\underline{\upsilon}, \underline{R}) \tag{4.2}$$

Where ($\underline{r}$) is the rate of consumption, ($\underline{\upsilon}$) is the reaction mechanism and ($\underline{R}$) the reaction rate.

4.3.1 Approach utilized

Two distinct approaches can be followed for kinetic studies: a differential approach and an integral approach. The integral approach focuses on the accumulation of concentrations over a specific period providing an overall view of the entire reaction process, highlighting the total change in concentrations from the start to the end of the reaction.
In contrast, the differential method aims to identify the instantaneous rates of reaction providing a more specific analysis, giving information about how concentrations change at a specific moment.
The approach employed in this study is the integral one. It allowed to predict the behavior through the integration of material balances.
The primary objective is to solve material balances as the one described in the *Equation 4.3*:

$$\frac{dc_i}{dt} = r_i \tag{4.3}$$

To solve analytically this equation, the experimental concentrations of the reactant are plotted over time. Then, the shape of the curves allows to make assumptions on the mechanism (ν) and the reaction rate (R).
The reaction rate is a function of the concentrations (c_i) and additional parameters and is given by the following *Equation 4.4*:

$$R = k{c_i}^{\alpha} \tag{4.4}$$

Where k is the kinetic constant of the reaction.
Considering the initial balance of the species i, the theorical material balance $c_i^{th}(t)$ can be solved thanks to the following system of equation (*Equation 4.5*):

$$\begin{cases} \dfrac{dc_i}{dt} = r_i = v_i R = -kc_i^{\alpha} \\ c_i(0) = c_i^0 \end{cases} \tag{4.5}$$

The experimental value $c_i^{exp}(t)$ is compared to the theoretical prediction $c_i^{th}(t)$ obtained using the assumed mechanism and rate.
The optimal parameters are those that approximate the best the average of all experimental data. To evaluate the accuracy of the used parameters, the absolute value of the difference between the experimental and theoretical concentrations evaluated simultaneously, shown in *Equation 4.6*, is introduced.

$$D = |c_i^{exp}(t) - c_i^{th}(t)| \tag{4.6}$$

The vector D comprises all the distances between experimental and theoretical concentrations. To combine these elements, a norm is applied. Following normalization, an objective function is formulated (*Equation 4.7*). D varies with the parameters in the model, and a lower D indicates a superior model. Therefore, parameter values should be selected to minimize the distance between the model and data.

$$F_{OBJ} = \left\| D_{i,exp-calc} \right\| = \sqrt{\sum_{i=1}^{N} {D_i}^2} \tag{4.7}$$

The objective function is then minimized using the *Excel* integrated function "*Solver*" by adjusting the different parameters. This process identifies the value that best fit with the experimental data.

To assess the accuracy of the objective function, a coefficient of determination (R^2) was introduced, which determined the proportion of variance in the dependent variable $c_i^{th}(t)$ that can be explained by the independent variable $c_i^{exp}(t)$.

In this study, a preliminary kinetic analysis was conducted incorporating certain assumptions. Generally, to achieve a comprehensive understanding of the actual reaction rate and mechanism, it is essential to sample and analyze reaction products at various time points. However, due to prolonged reaction times and the experimental setup, stopping the reaction at different intervals was impractical. Instead, identical reactions under the same conditions were conducted at various time intervals.

As a result, the kinetic study provided preliminary insights into how reactions with different catalysts operated. To determine the rate constant (k) and reaction rate, the concentration of the reactant in the final product was calculated from GC area peaks. Notably, variations in the initial concentration of the reactant occurred due to experimental errors. To address this, the initial concentration was averaged across different concentrations calculated for reactions conducted at various time intervals.

Following the previously explained procedure and incorporating the assumptions, the preliminary kinetic study of the HDO of eugenol reduction was conducted. Consequently, the proposed reaction rate is the one in *Equation 4.8*:

$$R = kc_{EUG}^{\alpha 1} c_{H_2}^{\alpha 2} \tag{4.8}$$

The kinetic constant, denoted as k, was associated with the concentrations of eugenol (c_{EUG}) and hydrogen (c_{H2}), represented by α1 and α2 as the exponents of the concentrations of the two reactants. As all experiments were conducted with an excess of H_2; for the sake of simplifying the kinetic study, it was assumed that the concentration of H_2 remains constant and was incorporated into the kinetic constant. Consequently, the reaction rate was expressed in *Equation 4.9*:

$$R = kc_{EUG}^{\alpha} \tag{4.9}$$

According to the previous assumptions, the corresponding material balance for the eugenol HDO is shown in the following *Equation 4.10*.

$$\frac{dc_{EUG}}{dt} = r_{EUG} = \nu_{EUG} R = -R \tag{4.10}$$

4.3.2 First order kinetics

To determine the order of the reaction of interest, concentration of the reactant was plotted over time for our different conditions (1M, 3M, 6M, 9M and 12M) (*Figure 4.12, Figure 4.13, Figure 4.14, Figure 4.15, Figure 4.16).* It was first assumed a first-order dynamic of the reaction.

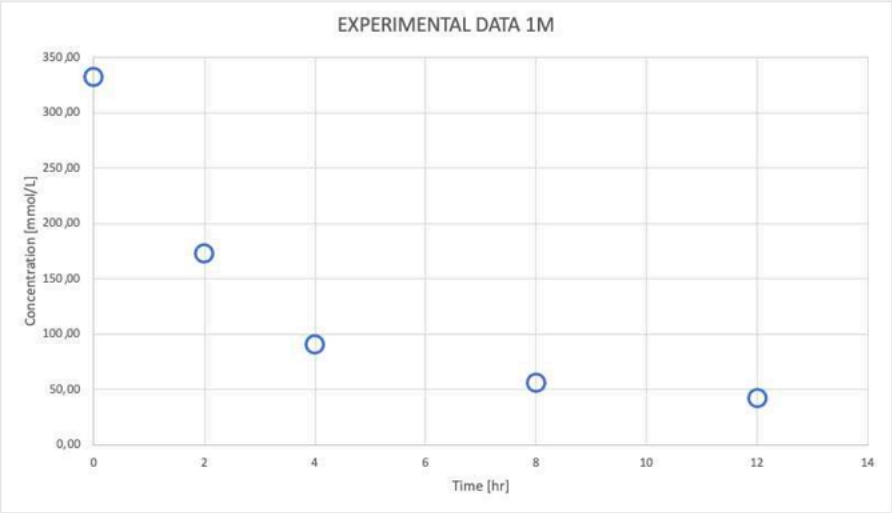

Figure 4.12 – Experimental data plot for 1M catalyst reactions at different time

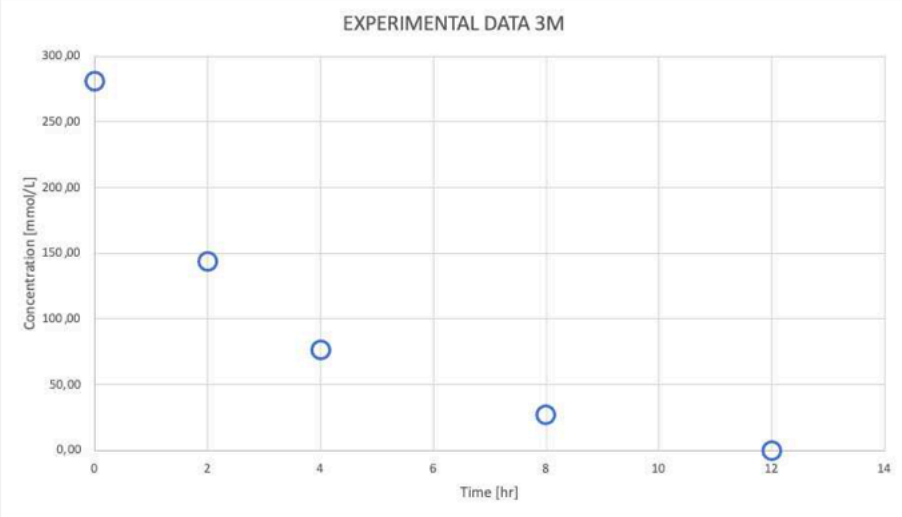

Figure 4.13 – Experimental data plot for 3M catalyst reactions at different time

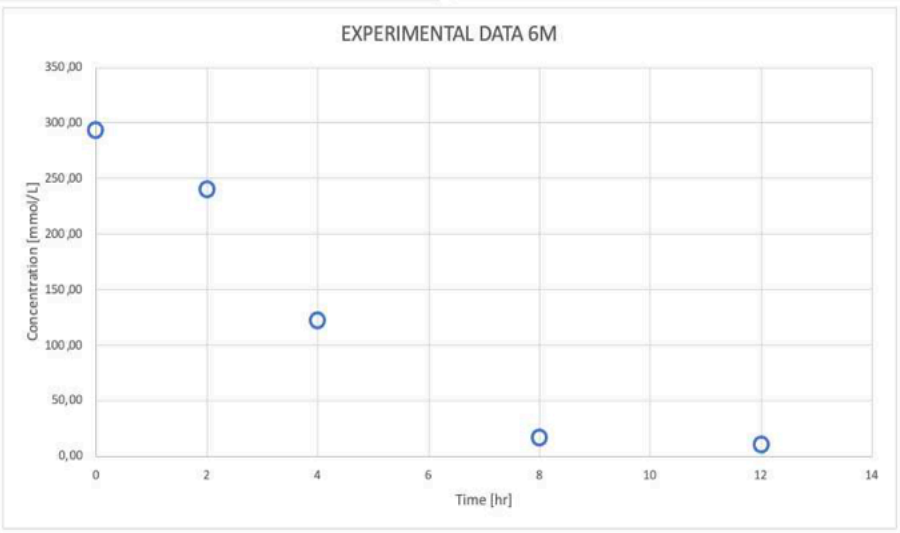

Figure 4.14 – Experimental data plot for 6M catalyst reactions at different time

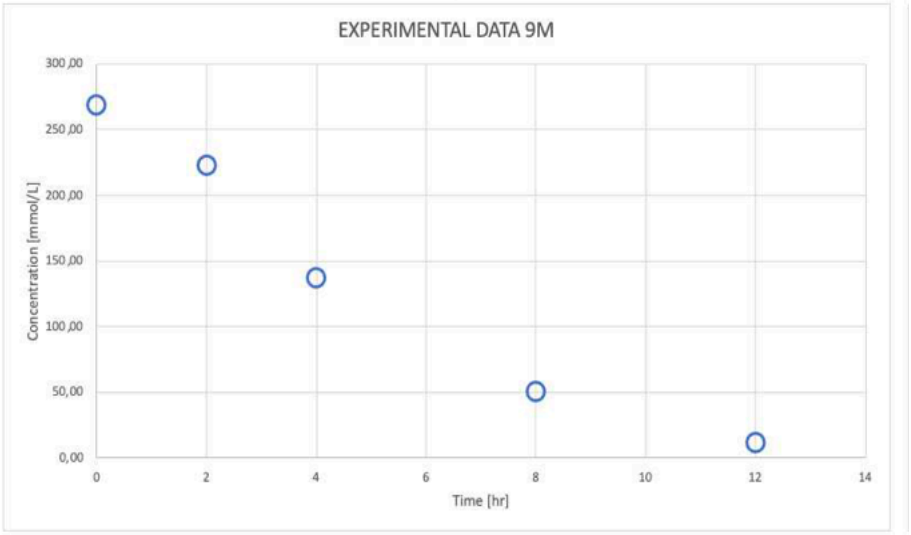

Figure 4.15 – Experimental data plot for 9M catalyst reactions at different time

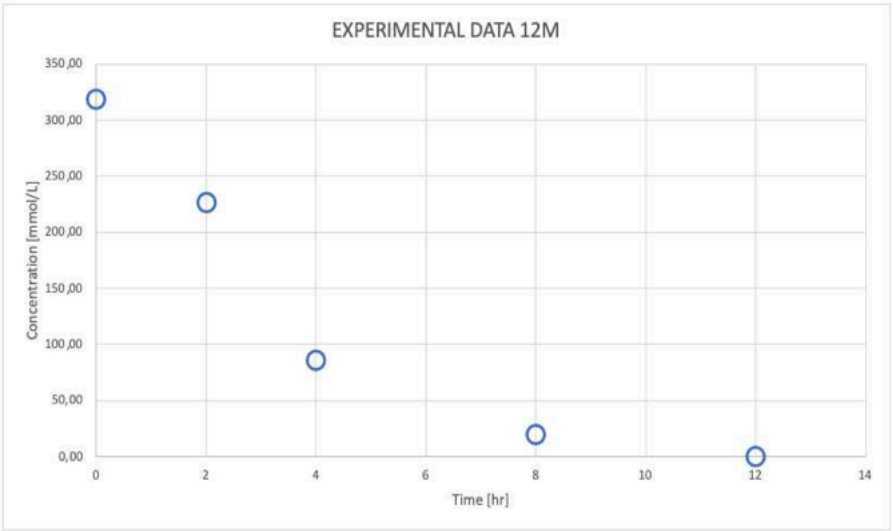

Figure 4.16 – Experimental data plot for 12M catalyst reactions at different time

Thus, α=1 was obtained. In this case, the material balance became (*Equation 4.11*):

$$\begin{cases} \frac{dc_{EUG}}{dt} = r_{EUG} = \upsilon_{EUG} R = -kc_{EUG} \\ c_{EUG}(0) = c_{EUG}^{0} \end{cases} \tag{4.11}$$

And the corresponding analytical solution was (*Equation 4.12*):

$$c_{EUG}^{th} = c_{EUG}^{0} \exp(-kt) \tag{4.12}$$

The first hypothesis was implemented in *Excel*, and an initial guess of the parameters was given. This allowed the estimation of the kinetic rate constant k and the R^2 of the regression for each curve.

Figure 4.17 – First order kinetics plot for 1M catalyst reactions

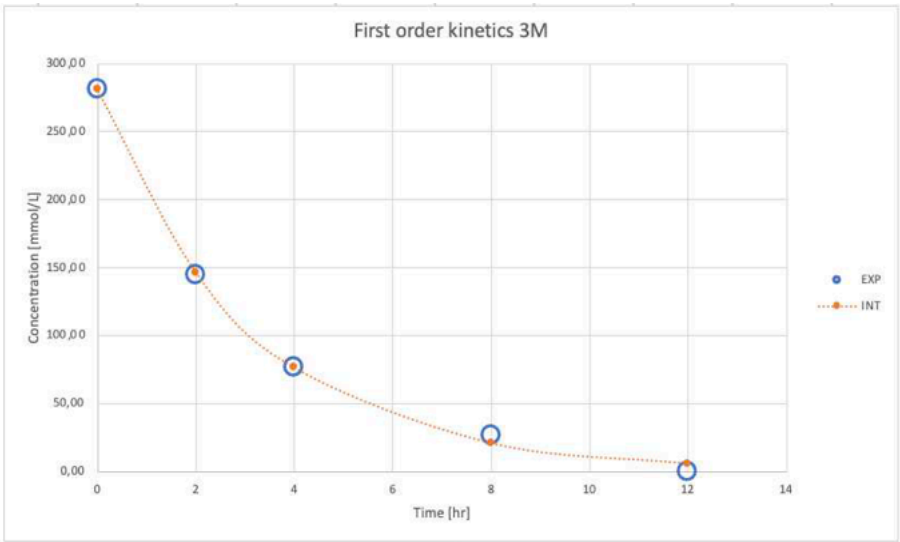

Figure 4.18 – First order kinetics plot for 3M catalyst reactions

Figure 4.19 – First order kinetics plot for 6M catalyst reactions

Figure 4.20 – First order kinetics plot for 9M catalyst reactions

Figure 4.21 – First order kinetics plot for 12M catalyst reactions

The initial guess and the final results for k are reported in *Table 4.2* and *Figure 4.17, Figure 4.18, Figure 4.19, Figure 4.20, Figure 4.21* showed the comparison between the experimental curve $c_{EUG}^{exp}(t)$ and the theoretical curve $c_{EUG}^{th}(t)$ with respect to the reaction time. It was observed that the calculated curve does not perfectly fit the experimental data, specifically for the 6M, 9M and 12M. It is also confirmed by the R^2 in *Table 4.2,* which is lower than the ones for 1M and 3M. It appears that the first order assumption approximates enough the kinetics of the reactions. The overall results didn't show a faster reaction compared to the others and the average kinetic constant was of 0.25 hr^{-1}.

Sample n°	**Initial Guess k [hr^{-1}]**	**Interpolated k [hr^{-1}]**	**R^2**
1M	0.5	0.2915	0.9807
3M	0.5	0.3262	0.9986
6M	0.5	0.2162	0.9569
9M	0.5	0.1773	0.9761
12M	0.5	0.2724	0.9723

Table 4.2 – Parameters of first order kinetics for the different reactions

Conclusions

This study aimed to develop a tri-component catalyst, $Ru/NbOPO_4/TiO_2$, under varying acidity conditions in the synthesis solutions. The goal was to understand the resulting catalyst's structural variations and its efficiency in the hydrodeoxygenation of depolymerized lignin products, specifically assessed with eugenol.

Examining the catalyst's structure synthesized under different acidity conditions revealed a more crystalline $NbOPO_4$ structure at higher HCl molar solutions (9M and 12M), contrasting with an amorphous structure at lower molarities (1M,3M,6M). The Lewis to Bronsted acid sites ratio increased with molarity. Notably, the mesoporous structure of TiO_2 contributed to the catalyst's stability, while the homogeneous distribution of Ru on the support enhanced acidity and activity.

Concerning the catalyst activity, the increase of acidity in the synthesis solution revealed no observable difference among the various catalysts, with the exception of the 1M, which showed lower conversion and yield. Catalysts from the 3M to 12M demonstrated consistent activity, high yield of the target product and of the fully saturated hydrocarbons.

The secondary goal was to mitigate the reaction conditions for the HDO reaction. While pressure was reduced from an average of 70 bars to 50 bars, a moderate change compared to previous studies, temperature was maintained at 200°C, contrasting with research typically conducted at much greater than 200°C and never under 225°C.

As already mentioned in *Section 4.2.6* future studies could explore less severe reaction conditions. Additionally, in order to explore the industrial potential of the catalyst an increase of the reactant-to-catalyst ratio can be applied, along with an increase of the reactor volume. This would give information about the actual costs the catalyst would have.

Finally, the catalyst can be employed in the conversion of lignin monomers and in lignin depolymerization to study its activity and efficiency on those fields.

Nomenclature

Acronyms:

ABS	= Acrylonitrile butadiene styrene
BET	= Brunauer - Emmett - Teller
BTX	= Benzene - Toluene - Xylene
DMSO	= Dimethyl sulfoxide
EDS/EDX	= Energy-dispersive X-ray
EUG	= Eugenol
FT-IR	= Fourier-Transform Infrared Spectroscopy
GC-FID	= Gas chromatography - Flame Ionization Detector
GC-MS	= Gas chromatography - Mass Spectroscopy
HDO	= Hydrodeoxygenation
HDPE	= High density Polyethylene
NbP	= $NbOPO_4$
P123	= Poly(ethylene glycol)-block-poly(propylene glycol)-block-poly(ethylene glycol)
PBS	= Polybutylene succinate
PET	= Polyethylene terephthalate
PXRD	= Powder X-ray diffraction
SBA-15	= Santa Barbara Amorphous - 15
SEM	= Scanning Electron Microscope
SIM	= Selected Ion Monitoring
TEM	= Transmission Electron Microscopy
TPD	= Temperature-Programmed Desorption

Symbols:

c	= Concentration
D	= Distance from values
G	= Guaiacyl monomer
H	= Coumaryl monomer
k	= kinetic constant
m	= Mass

MW = Molecular weight
R = Rate of reaaction
r = Rate of production
R^2 = Coefficient of determination
S = Syringyl monomer
T = Temperature
t = Time

Greek letters:

v = Reaction mechanism

Bibliography

[1] Armah, Edward Kwaku, et al. *Biotechnological Applications of Biomass*. IntechOpen, 2020

[2] Kumar, A., Anushree, Kumar, J., Bhaskar, T., 2020. *Utilization of lignin: a sustainable and eco-friendly approach*. J. Energy Inst 93, 235-271.

[3] González-González, Reyna Berenice, et al. "(Re)-thinking the bio-prospect of lignin biomass recycling to meet sustainable development goals and circular economy aspects." *Current Opinion in Green and Sustainable Chemistry* (2022): 100699.

[4] Bilal, Muhammad, et al. "Exploring the potential of ligninolytic armory for lignin valorization–A way forward for sustainable and cleaner production." *Journal of Cleaner Production* 326 (2021): 129420.

[5] Esquivel Hernández, Diego & García, Saul & Lopez Pacheco, Itzel & Iqbal, Hafiz & Parra, Roberto. (2022). *Resource recovery of lignocellulosic biomass waste into lactic acid - Trends to sustain cleaner production*. Journal of Environmental Management. 301. 113925. 10.1016/j.jenvman.2021.113925.

[6] Luo, H., Abu-Omar, M.M., 2017. *Chemicals from Lignin. Encycloded SuS Technol*. Elsevier, ISBN 9780128046777, pp. 573-585

[7] Mandlekar, N., Cayla, A., Rault F., Giraud, S., Salaün, F., Malucelli, G., Guan, J.P., 2018. *An overview on the use of lignin and its derivatives in fire retardant polymer systems*. Lignin-Trends Appl. 207,231.

[8] Bajwa, D. S., Pourhashem, G., Ullah, A. H., & Bajwa, S. G. (2019). A concise review of current lignin production, applications, products and their environmental impact. *Industrial Crops and Products*, *139*, 111526.

[9] Margellou, A., & Triantafyllidis, K. S. (2019). Catalytic transfer hydrogenolysis reactions for lignin valorization to fuels and chemicals. *Catalysts*, *9*(1), 43.

[10] Ambursa, M. M., Juan, J. C., Yahaya, Y., Taufiq-Yap, Y. H., Lin, Y. C., & Lee, H. V. (2021). A review on catalytic hydrodeoxygenation of lignin to transportation fuels by using nickel-based catalysts. *Renewable and Sustainable Energy Reviews*, *138*, 110667.

[11] Mortensen, P. M., Gardini, D., Damsgaard, C. D., Grunwaldt, J. D., Jensen, P. A., Wagner, J. B., & Jensen, A. D. (2016). Deactivation of Ni-MoS2 by bio-oil impurities during hydrodeoxygenation of phenol and octanol. *Applied Catalysis A: General*, *523*, 159-170.

[12] Gutierrez, A., Turpeinen, E. M., Viljava, T. R., & Krause, O. (2017). Hydrodeoxygenation of model compounds on sulfided CoMo/γ-Al2O3 and NiMo/γ-Al2O3 catalysts; Role of sulfur-containing groups in reaction networks. *Catalysis Today*, *285*, 125-134.

[13] Selvaraj, M., Shanthi, K., Maheswari, R., & Ramanathan, A. (2014). Hydrodeoxygenation of guaiacol over MoO3-NiO/mesoporous silicates: Effect of incorporated heteroatom. *Energy & fuels*, *28*(4), 2598-2607.

[14] Samikannu A, Konwar LJ, Rajendran K, Lee CC, Shchukarev A, Virtanen P, et al. Highly dispersed NbOPO4/ SBA-15 as a versatile acid catalyst upon production of renewable jet-fuel from bio-based furanics via hydroxyalkylation-alkylation (HAA) and hydrodeoxygenation (HDO) reactions. Appl Catal B Environ 2020. https://doi.org/10.1016/j.apcatb.2020.118987.

[15] N. K. Shammas and L. K. Wang, Vacuum filtration. In: *Biosolids Treatment Processes*, pp. 495–518. L. K. Wang, N. K. Shammas, and Y. T. Hung (eds.), Humana Press, Inc., Totowa, NJ (2007).

[16] JoVE Science Education Database. Organic Chemistry. Rotary Evaporation to Remove Solvent. JoVE, Cambridge, MA, (2023).

[17] Britannica, The Editors of Encyclopaedia. "calcination". *Encyclopedia Britannica*, 15 Nov. 2021, https://www.britannica.com/technology/calcination. Accessed 4 November 2023.

[18] Hwang, N.; Barron, A.R. *BET Surface Area Analysis of Nanoparticles*; Rice University: Houston, TX, USA, 2021.

[19] Kruk M.; Jaroniec M. Gas adsorption characterization of ordered organic-inorganic nanocompsite materials. Chem. Mater. 2001.

[20] Chauhan A, Chauhan P. Powder XRD technique and its application in science and technology. J Anal Bioanal Tech. 2014;5:1-5.

[21] Ermrich, M., & Opper, D. (2013). XRD for the analyst. Getting acquainted with the principles. Second. Panalytical.

[22] Yani, Firda Tirta, et al. *Journal of Cleaner Production* 354 (2022): 131704. (2) Castro, Douclasse C., et al. *Journal of the Brazilian Chemical Society* 27 (2016): 303-313

[23] Z. Bacsik, J. Mink, G. Keresztury, FTIR Spectroscopy of the Atmosphere. I. Principles and Methods, Appl. Spectrosc. Rev. 39 (3) (2004)

[24] Joy, David C., Bradbury, Savile and Ford, Brian J.. *"scanning electron microscope". Encyclopedia Britannica*, 12 Oct. 2023.

[25] Egerton, R. F. (2005) Physical principles of electron microscopy : an introduction to TEM, SEM, and AEM. Springer, 202.

[26] Goldstein, J. (2003) Scanning electron microscopy and x-ray microanalysis. Kluwer Adacemic/Plenum Pulbishers, 689 p.

[27] *Transmission electron microscopy*, David B. Williams and C. Barry Carter (Plenum, 1996)

[28] *Electron microscopy of thin crystals*, Peter Hirsch (Butterworths, 1965)

[29] Si, Z., Weng, D., Wu, X., Yang, J., & Wang, B. (2010). Modifications of CeO2–ZrO2 solid solutions by nickel and sulfate as catalysts for NO reduction with ammonia in excess O2. *Catalysis Communications*, *11*(13), 1045-1048.

[30] Xie, G., Liu, Z., Zhu, Z., Liu, Q., Ge, J., & Huang, Z. (2004). Simultaneous removal of SO2 and NOx from flue gas using a CuO/Al2O3 catalyst sorbent: II. Promotion of SCR activity by SO2 at high temperatures. *Journal of Catalysis*, *224*(1), 42-49.

[31] Yani, F. T., Husin, H., Muhammad, S., Abnisa, F., & Nasution, F. (2022). Palm oil hydrodeoxygenation into green diesel over NiO/NbOPO4 catalyst: A novel approach of synthesizing NbOPO4 from NbCl5. *Journal of Cleaner Production*, *354*, 131704.

[32] Pereira, Paulo & Voorwald, Herman & Cioffi, Maria Odila & Silva, M. & Rego, Ana Maria & Ferraria, Ana & Pinho, Maria. (2014). Sugarcane bagasse cellulose fibres and their hydrous niobium phosphate composites: Synthesis and characterization by XPS, XRD and SEM. Cellulose. 21. 10.1007/s10570-013-0113-2.

[33] Dong, W., Sun, Y., Lee, C.W., Hua, W., Lu, X., Shi, Y., Zhang, S., Chen, J., Zhao, D., 2007. Controllable and repeatable synthesis of thermally stable Anatase NanocrystalSilica composites with highly ordered hexagonal mesostructures. J. Am. Chem. Soc. 129 (45), 13894e13904.

[34] Kao, L. H., Hsu, T. C., & Cheng, K. K. (2010). Novel synthesis of high-surface-area ordered mesoporous TiO2 with anatase framework for photocatalytic applications. *Journal of colloid and interface science*, *341*(2), 359-365

[35] Calleja, G., Serrano, D. P., Sanz, R., Pizarro, P., & García, A. (2004). Study on the synthesis of high-surface-area mesoporous TiO2 in the presence of nonionic surfactants. *Industrial & engineering chemistry research*, *43*(10), 2485-2492.

[36] Bartle, K. D., & Myers, P. (2002). History of gas chromatography. *TrAC Trends in Analytical Chemistry*, *21*(9-10), 547-55

[37] Poole CF. Ionization-based detectors for gas chromatography. J Chromatogr A. 2015 Nov 20;1421:137-53. doi: 10.1016/j.chroma.2015.02.061. Epub 2015 Feb 24. PMID: 25757823.

[38] Bjelić, A., Grilc, M., & Likozar, B. (2018). Catalytic hydrogenation and hydrodeoxygenation of lignin-derived model compound eugenol over Ru/C: Intrinsic microkinetics and transport phenomena. *Chemical Engineering Journal*, *333*, 240-259.

[39] Sulman, A., Mäki-Arvela, P., Bomont, L., Alda-Onggar, M., Fedorov, V., Russo, V., ... & Murzin, D. Y. (2019). Kinetic and thermodynamic analysis of guaiacol hydrodeoxygenation. *Catalysis Letters*, *149*, 2453-2467.

Acknowledgments

First of all, I would like to thank Professor Paolo Canu for giving me the opportunity to carry out my thesis work in Sweden at Umeå University and for assisting me during the project. I would also like to thank Professor Jyri-Pekka Mikkola, Ajaikumar Samikannu, and Minh Van Dinh for supporting me at all times of need and guiding me during the experimental work.